Investigation of Core Failure during Excavation

A THESIS
SUBMITTED TO THE FACULTY OF THE GRADUATE SCHOOL
OF THE UNIVERSITY OF MINNESOTA
BY

Stephen Thomas Wilk

IN PARTIAL FULFILLMENT OF THE REQUIREMENTS
FOR THE DEGREE OF
MASTER OF SCIENCE

Professors Joseph F. Labuz and Charles Fairhurst

August 2012

Abstract

An increasing need to determine the *in-situ* stress state through indirect methods such as core disking has spawned much research over the past few years. While laboratory and field work have brought knowledge to the topic, many issues associated with these approaches have led to a reliance on numerical models for analysis. It is imperative that these numerical methods replicate the failure process and disk thicknesses, which are then related to a component of the *in-situ* stress state.

The constitutive model of tensile softening was used to both replicate previous laboratory experiments and match the general relation between disk thickness and major principal stress. The failure process was analyzed in detail for various stress magnitudes along with size effect. Also, laboratory experiments involving the excavation of cores in a stressed rock were performed to investigate the effect of core damage on measured elastic parameters. It was determined that when the vertical stress $\sigma_v = 0$ and horizontal stresses $\sigma_H = \sigma_h = 75 - 85\%\ C_o$, where C_o = uniaxial compressive strength, Young's modulus can decrease about 10% from the coring process.

Table of Contents

List of Tables

List of Figures

Chapter 1: Introduction

1.1 Motivation

In-situ stress determination remains an important issue for underground design and limitations in traditional methods have led to the exploration of various indirect means, such as core disking, to help estimate the *in-situ* stress state. Due to the complexity of the core disking process and difficulty of laboratory tests, numerical methods are being used to simulate the disking phenomenon. A numerical analysis replicating experimental work has already been accomplished, but new field studies suggest the results may only apply to a certain range of stresses. Therefore, it is unclear whether numerical models can simulate core disking effects for a wide range of stress magnitudes or be used as predictive tools. This thesis is an attempt to address these issues by investigating the effects of core damage and their relation to the *in-situ* stress state by implementing various failure criteria and constitutive models using the software FLAC. A detailed analysis of the failure process and important features then follow.

1.2 Objective

The main objectives of the thesis are to:

- establish an appropriate constitutive model for core disking that can simulate the failure process involving disk thickness and stress magnitude;
- determine if core damage can significantly change elastic parameters through experimental means;
- investigate the use of numerical methods as predictive tools of the *in-situ* stress state associated with core disking

1.3 Scope and Organization

All core excavations analyzed are associated with axisymmetric biaxial loading - horizontal stresses are equal and vertical stress is zero - and only the mechanical effect from excavation will be considered. More complex stress states will produce various types of core fractures. Thermal, fluid, and tool effects are likely to influence the disking process, but due to the complexity of core disking, it is important to understand the basic scenarios before advancing to more complex analyses.

The thesis is organized into five chapters. Chapter 2 presents a detailed literature review of core disking along with all experimental related material. Chapter 3 introduces the numerical model. After an explanation of model setup, an elastic analysis is performed to determine how stress distributions and magnitudes change during the excavation process. Then, the Mohr-Coulomb and Hoek-Brown failure criteria are introduced along with relevant plasticity concepts. Chapter 4 presents the results of the numerical analyses. An appropriate constitutive model for core disking is established. Then, a detailed analysis of the failure process is presented. Size effect analyses are performed after. Finally, the presence of core damage in intact cores is investigated along with preliminary predictions of the experiment. Chapter 5 presents a summary of findings along with conclusions and potential future work.

Chapter 2: Background and Experiments

2.1 Literature Review

In the next few decades, it is expected that the recent trend of deep underground projects, whether it be mining, petroleum, or infrastructure related, will continue. Two challenges that arise at excavation depths of thousands of meters are measuring the in-situ stress state and ensuring that rock properties found in the laboratory reflect those of the rock mass. Improper estimates of either can lead to unexpected failures, forcing companies to spend time and money to redo and repair designs.

The field of rock mechanics is unique in the sense that tested material must first be excavated from a stressed medium. The retrieval process unloads the core, redistributing stresses and potentially damaging the rock. Depending on stress magnitudes, this damage may range from microcracks, possibly changing material properties, to core separating fractures. Also, when in-situ stresses are large, traditional methods of measuring these stresses, such as hydraulic fracturing, encounter problems and may be unable to measure the stress state. This has led researchers to investigate alternative means of measuring the in-situ stress state through indirect methods such as borehole breakouts and drilling induced fractures [1,2].

2.1.1 Core Disking

While excavating in highly stressed rock, e.g. subject to stresses greater than 50% of the uniaxial compressive strength, the redistribution of stress may cause the core to fracture in various ways depending on the stress state [3]. For example, horizontal fracturing at regular intervals, called core disking, is attributed to regions of high horizontal stresses, or thrust fault environments. Equal horizontal stresses will cause flat disking while unequal horizontal stresses generally cause saddle-shaped disks. The distance of the fracture interval, called disk thickness, has been observed to decrease with increasing horizontal stress magnitudes, leading to the conclusion that the disk thickness can be related to the in-situ stress state [4].

In attempts to determine a disking – in-situ stress relation, multiple core disking research projects have been performed in the past 50 years. Jaeger and Cook initially conducted core disking laboratory experiments and discovered that disk thickness does change with the applied stress state, setting the stage for future research on the topic [4]. Obert and Stephenson extended Jaeger and Cook's work, performing experiments with an axisymmetric triaxial testing machine on various types of rock, formulating a disking criterion that relates the radial and axial stresses causing disk initiation [5]. Over the next 40 years, multiple axisymmetric and three dimensional (elastic) numerical models were used to identify possible core disking failure mechanisms and some even created their own disking criterion relating disk thickness to the in-situ stress state [6-11]. Recently, with the increase in computing power and numerical modeling sophistication, elasto-plastic models have given more detailed insight into the core disking process [12-16]. Field studies and experiments have also been performed throughout the past 50 years, giving valuable information about factors affecting disking and the predictability of proposed disking criteria [17-22].

From this work, many notable accomplishments have been achieved. Field studies at the URL in Canada gives a full relation between disk thickness and major principal stress (σ_1) for Lac du Bonnet granite and granodiorite [22]. Numerical models have simulated the change in stress distribution in the core as the excavation proceeds, leading to the consensus that core disking results from a tensile failure mechanism [3,12,14-16]. Also, elasto-plastic numerical models have simulated experimental disk thickness results within a few percent [13].

Despite these accomplishments, no disking criterion has repeatedly shown success relating disk thickness with the stress state. Corthésy and Leite, who replicated Obert and Stephenson's experimental results and performed a detailed parametric analysis on core disking, suggested that disking is sensitive to material parameters, geometry, and external factors, so any disking criterion would be insufficient in predicting in-situ stress states [13]. Therefore, it was later suggested that individual circumstances (material properties, geometry, fluid pressure, thermal effects, *etc.*) should be

incorporated in an elasto-plastic numerical model [15]. By doing this, various stress states can be simulated until the numerical and physical disk thicknesses match, ideally giving an estimate of the physical stress state.

Yet, before numerical approaches can be implemented, it is imperative that the software can replicate the basic mechanism behind disking. While the disking phenomenon has been replicated for stress magnitudes slightly above the disking initiation stress, the stress limit that must be achieved in order for disking to occur, shear failure modes have controlled for higher stress levels instead of the expected tensile failure mode [13,15]. This switch to a shear failure mode has not been observed in field or laboratory results [22], questioning the ability of these models to replicate disking.

2.1.2 Core Damage

While recognized as an issue [1,23-27], the field of rock mechanics largely ignores the influence of damage from the excavation process on material properties. Excavation procedures are executed without taking the integrity of the core into account. At lower stress levels, this proves not to be an issue because stresses are not large enough to damage the rock upon unloading. However, at higher stress levels, core fractures sometimes appear, bringing up the question of whether damage occurred at stress levels below the disking initiation stress.

2.2 Experimental Setup

Core disking experiments were performed within a hydraulic fracturing apparatus. The testing machine originally allows a 17 x 17 x 17 cm cube of rock to be laterally loaded with oil pressure from flat-jacks, but had to be modified with removable aluminum sheets to accommodate the specimen size of 16 x 16 x 16 cm. The flat-jacks are

designed to support pressure up to 20 MPa and can accommodate both equal and unequal horizontal stress states.

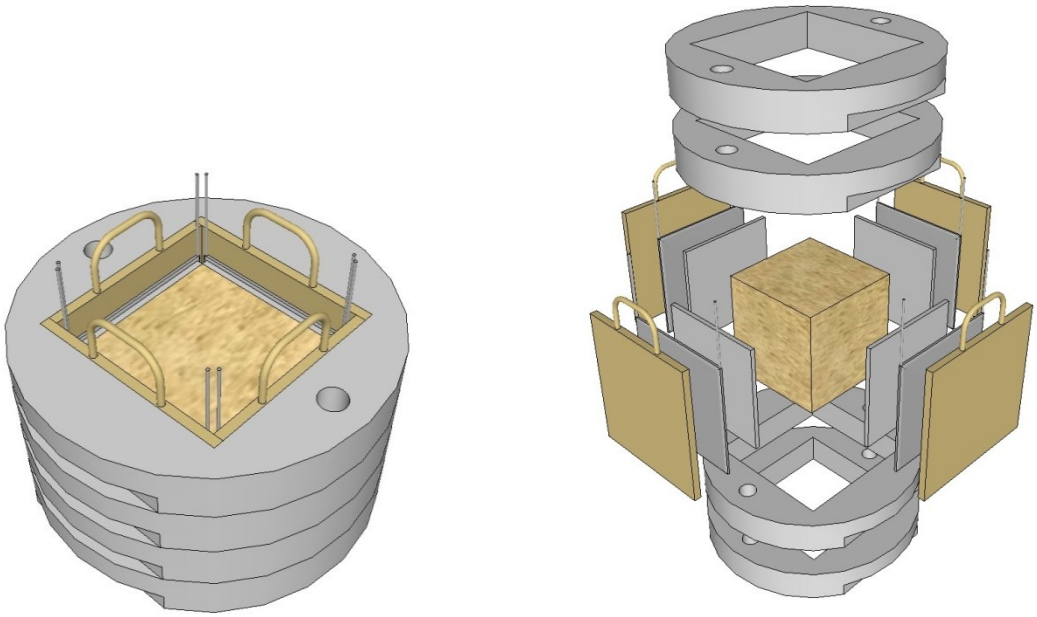

Figure 2.1: Diagram of hydraulic fracturing apparatus (Courtesy of Derrick Blanksma).

Due to limitations of the lateral stress magnitude, a weak rock is required to produce disking. Laboratory and field studies suggest the disking initiation stress is usually 6 – 10 times the tensile strength [5,22]. This implies that the rock must have a tensile strength of less than 2 – 3 MPa.

Two different rocks were used in the core disking experiments. Calcarenite, a calcareous sedimentary rock composed of detrital particles, and Boise sandstone, an anisotropic sandstone, were selected due to their low tensile strengths and known material parameters. Grain sizes are similar for both rocks, ranging from 0.06 – 2 mm. However, large shells were observable in the Calcarenite without the use of a microscope.

Three blocks (16 x 16 x 16 cm) of Calcarenite and a single block (17 x 17 x 17 cm) of Boise sandstone were tested. It should be noted that the Boise test was considered preliminary and was performed to check the experimental process. The limited number of tests does not allow any relations to be developed due to statistical significance, but the tests can still be useful in observing core disking and damage.

One advantage of using Calcarenite is that the material parameters have been thoroughly characterized for a different block of Calcarenite [28]. The material parameters of Boise sandstone were determined using uniaxial compression, triaxial compression, and uniaxial tensile tests. Table 2.1 displays the results.

Table 2.1: Strength properties of Calcarenite and Boise sandstone [28].

Material	Young's modulus	Poisson's ratio	Cohesion	Friction angle	UCS	Tensile strength
	[GPa]	[MPa]	[MPa]	[°]	[MPa]	[MPa]
Calcarenite	8.35	0.237	5.62	22	16.1	2.07
Boise sandstone (parallel)	10.0	0.25	9.46	23	28.8	2.5
Boise sandstone (perpendicular)	10.0	0.25	5.37	41	23.5	-

Since core disking involves a tensile failure mechanism (mode I fracture), three-point bending tests were performed to measure the modulus of rupture (σ_t) and fracture toughness (K_{IC}). Both rocks were cut into two beams, both around 55 x 20 x 160 mm. A notch, 3.5 mm in length, was cut at the midspan of one of the beams. Both beams were loaded to failure and the peak load was used to determine the σ_t and K_{IC}:

$$\sigma_t = \frac{3PS}{2bh^2} \tag{2.1}$$

$$K_{IC} = \frac{PS}{bh^{3/2}} * f\left(\frac{a}{h}\right) \tag{2.2}$$

$$f\left(\frac{a}{h}\right) = 3\sqrt{\frac{a}{h}} * \frac{1.99 - \left(\frac{a}{h}\right)\left(1 - \frac{a}{h}\right)\left[2.15 - 3.93\left(\frac{a}{h}\right) + 2.7\left(\frac{a}{h}\right)^2\right]}{2\left(1 + \frac{2a}{h}\right)\left(1 - \frac{a}{h}\right)^{\frac{3}{2}}} \tag{2.3}$$

P is load at failure, *S* is span of beam, *b* is width, *h* is height, and *a* represents the notch length. σ_t and K_{IC} were determined to be 2.92 MPa and 0.24 MPa*m$^{1/2}$ respectively for Calcarenite and 3.5 MPa and 0.42 MPa*m$^{1/2}$ for Boise sandstone. Assuming linear elastic fracture mechanics, the fracture energy can be determined using the following equation.

$$G_f = \frac{{K_I}^2}{E} \tag{2.4}$$

This gives fracture energies of 6.73 and 17.3 J/m^2 for the Calcarenite and Boise sandstone respectively. It should be noted that only two fracture tests were performed on each rock.

To compare the elastic parameters of the Calcarenite block with values found by Meyer [28], ultrasonic methods were used. The ultrasonic velocities followed ASTM D 2845-08 standards. Both P- and S-waves can be generated and transmitted through the rock, allowing a user to determine the arrival time for both waves. The speeds of both P- and S-waves are defined in equations (2.5) and (2.6):

$$c_p = \frac{L}{t_p} \tag{2.5}$$

$$c_s = \frac{L}{t_s} \tag{2.6}$$

The elastic parameters can be determined with the following equations:

$$E = \frac{\rho c_s^2 (3c_p^2 - 4c_s^2)}{(c_p^2 - c_s^2)} \tag{2.7}$$

$$\upsilon = \frac{(c_p^2 - 2c_s^2)}{2(c_p^2 - c_s^2)} \tag{2.8}$$

For each 16 x 16 x 16 cm block, four P-wave velocities, all through different regions of the block, and one S-wave velocity was taken for each of the three Cartesian directions. The results are presented in Table 2.2.

Table 2.2: P- and S-wave velocities, Young's modulus, and Poisson's ratio for three directions of the three blocks of Calcarenite.

Block	$c_p(x)$	$c_p(y)$	$c_p(z)$	$c_s(x)$	$c_s(y)$	$c_s(z)$
1	3397	3369	3361	2037	1199	2053
2	3379	3374	3415	2065	2065	2095
3	3344	3394	3365	2050	2087	2043
	E [GPa]			υ		
1	20.14	19.53	20.16	0.219	0.228	0.202
2	20.34	20.32	20.88	0.202	0.201	0.199
3	19.95	20.63	19.96	0.199	0.196	0.208

Assuming isotropic behavior, Young's modulus and Poisson's ratio are found to be 20.35 GPa and 0.20. Comparing with the results of Meyer [28], Young's modulus is doubled and Poisson's ratio differs by 0.037. While this is not surprising since the rock label "Calcarenite" represents a wide range of rocks with varying elastic and strength values, it was of concern since not enough rock was available to test strength properties of the new batch of Calcarenite. It was assumed that the strength properties are the same when determining the stress levels for the experiment.

To conduct the disking experiments, the block of rock was first placed inside the hydraulic fracturing apparatus. The apparatus only allows two flat-jacks, opposite from each other, to be loaded at a time. To avoid large unequal horizontal stress states, the loading and unloading occurred in two increments, switching to adjacent sides after each increment. Once loaded, the block of rock was cored slowly, at 0.5 mm/min, using a 31.5 mm diameter water cooled diamond bit drill until the midheight was reached. Once at the midheight, the drill was removed and the specimen was examined.

2.3 Experimental Results

The three Calcarenite blocks were tested at various stress magnitudes: 4.8 σ_t (10 MPa), 5.8 σ_t (12 MPa), and 6.8 σ_t (14 MPa) with the numerical prediction that disking would occur at 5.3 σ_t (11 MPa) (Chapter 4.7). The Boise sandstone block was tested at 7 σ_t (17.5 MPa). Because of the bedding planes in Boise sandstone, it was decided to drill perpendicular to the bands in hopes that disking would be promoted, but the full effect of the anisotropy is unknown.

Disking was observed in the Boise sandstone specimen, but not in the regular interval pattern that is commonly observed. After excavating a depth of 6 R (90 mm), two disks formed. The disk between the disk fracture and free surface had a thickness of 3.37 R (52.2 mm) and the second disk had a thickness of 0.403 R (6.3 mm). A third section of the core, 2 R (31.5 mm), also exists but it is difficult to tell if the separating fracture at the bottom was drilling induced or a result of removing the core. Both fractures had an upward curvature and damage could be observed on the lower part of the first disk and the top part of the third section of core. The disking fractures and damage seemed to occur within the lighter region of the sandstone, implying a weak area within the rock.

Figure 2.2: Photo of core disking in Boise sandstone

Core disking was not observed in the Calcarenite samples. While an attempt was made to produce at least one disked sample, it was impossible to predict the disking initiation

stress since the particular Calcarenite specimen was not characterized. It also has been observed that disking does not appear in some weak rocks, such as South Dakota Chalk (UCS = 12 MPa) [5], which displays similar strength properties to the Calcarenite. However, core disking was observed in different tuffaceous rocks (uniaxial compressive strength = 6.4 – 16.1 MPa) [20] and in the Boise sandstone. As mentioned, disk initiation occurs at around 6-10 σ_t so a rock with a tensile strength of 2.07 MPa would require 12 – 20 MPa to disk. Without more samples, it is impossible to determine whether disking cannot occur in Calcarenite or the stress magnitudes were too low.

Even though disking was not produced in the Calcarenite samples, it is possible to test for damage and a change in elastic parameters after coring in a stressed medium. To isolate the effect from drilling, a second core (Core B) was taken from each block after unloading. Previous research suggests that wave velocities and Young's modulus should decrease with increasing damage while the crack closure threshold (σ_{cc}) should increase [23].

Ultrasonic velocities and mechanical testing were performed to check if signs of damage are observed. P- and S- wave velocities were determined and the resulting elastic parameters were calculated. The mechanical testing consisted of loading the core uniaxially until a linear response was reached, around 0.5 C_o (7 – 8 MPa), and then unloaded.

From the stress-strain curves (Appendix A), the loading and unloading Young's modulus could be determined. To keep consistency, the linear region was assumed to be between 0.3 – 0.5 C_o (5 - 8 MPa). The crack closure threshold was identified by the location where the slope of the stress-strain curve remains constant. Since the force-displacement values were recorded every second, a range of ten seconds was used to calculate the slope, eliminating the effect from minor oscillations in loading.

$$E_i = \frac{(\sigma_{i+5} - \sigma_{i-5})}{(\varepsilon_{i+5} - \varepsilon_{i-5})} \tag{2.9}$$

Appendix A contains figures relevant to the threshold determination. From a loading-unloading curve, the energy loss (ΔU) per volume from hysteresis can also be calculated by integrating the area enclosed by the stress-strain curve. The maximum stress for each core does vary, which affects the results, so any energy loss above the lower maximum stress of the two cores for any loading condition was dismissed.

Tables 2.3 and 2.4 display the results from the ultrasonic and mechanical loading methods respectively. Figures 2.5 - 2.7 show the stress-strain curves for the loading-unloading cycles for all three loading conditions: 10, 12, and 14 MPa. To reiterate the definitions used, "Core A" means the core was taken while the block was laterally loaded. "Core B" means the block was laterally loaded then unloaded before coring. Since damage was expected to occur during the loading process, the control core was taken after unloading to isolate the damage due to the excavation process.

Table 2.3: P- and S-wave velocities, Young's Modulus, and Poisson's ratio of six Calcarenite cores. Core A specimens were cored under loaded conditions while the Core B specimens were cored under no load conditions. Loading condition specifies the stress magnitude that the core experienced.

Parameter		Core A			Core B		
		10 MPa	12 MPa	14 MPa	10 MPa	12 MPa	14 MPa
c_p	[m/s]	3329	3467	3418	3225	3387	3439
c_s	[m/s]	2224	2085	2018	1985	2128	2044
E	[GPa]	7.12	6.96	6.33	5.31	7.72	7.22
υ	[-]	0.097	0.217	0.232	0.195	0.174	0.227

From Table 2.3, significant decreases in P- and S-wave velocities are not observed, with values consistently around 3300 – 3450 m/s for c_p and 2000 – 2200 for c_s. S-wave velocities did decrease slightly for 12 and 14 MPa, 2128 to 2085 m/s and 2044 to 2018 m/s, and it is possible that decreases in c_p did not occur due to the small applied seating load during examination. P-wave velocities should only be affected if cracks are open so a small load may close the cracks, allowing the P-wave to propagate as if the rock was intact.

Due to the decrease in c_s for the 12 and 14 MPa specimens, the calculated Young' modulus does slightly decrease. For 12 MPa, Young's modulus decreases from 7.72 to 6.96 GPa, a 9.84% difference, and 7.22 to 6.33 GPa, a 12.3% difference, for 14 MPa. The 10 MPa loading condition showed a large increase in Young's modulus, from 5.31 GPa to 7.12 GPa, suggesting that the unstressed 10 MPa block was damaged from other sources. It should also be observed that the Young's Modulus of the stressed block did decrease with increasing applied stress, from 7.12 to 6.96 to 6.33 GPa, even though P-wave velocities showed an opposite trend, 3329 to 3467 to 3418 m/s. Figure 2.3 presents the data.

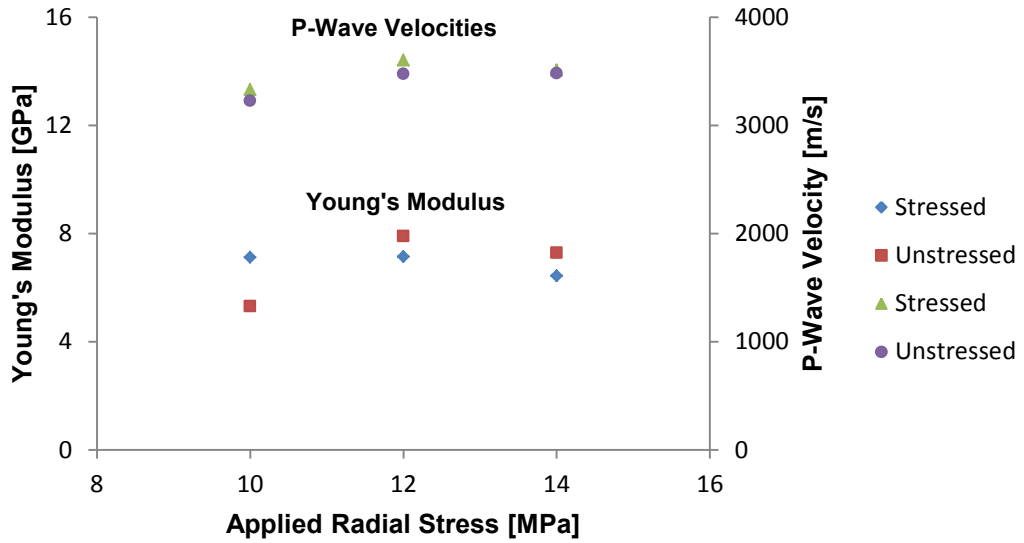

Figure 2.3: Comparison of stress and unstressed values of Young's modulus and P-wave velocity. Core A specimens were excavated under loaded conditions while Core B specimens were excavated under no load conditions. Loading condition specifies the stress magnitude that the core experienced.

Table 2.4: Comparison of Young's modulus in loading (E_L) and unloading (E_U), crack closure threshold (σ_{cc}) and energy loss (ΔU).

Young's modulus		Core A			Core B		
		10 MPa	12 MPa	14 MPa	10 MPa	12 MPa	14 MPa
E_L	[GPa]	10.60	9.17	9.11	4.37	13.00	9.78
E_U	[GPa]	13.74	12.71	13.01	10.44	16.96	15.19
σ_{cc}	[MPa]	5.28	5.82	5.13	1.03	5.18	0.508
ΔU	[J/m^3]	0.634	0.655	0.804	3.15	0.425	0.639

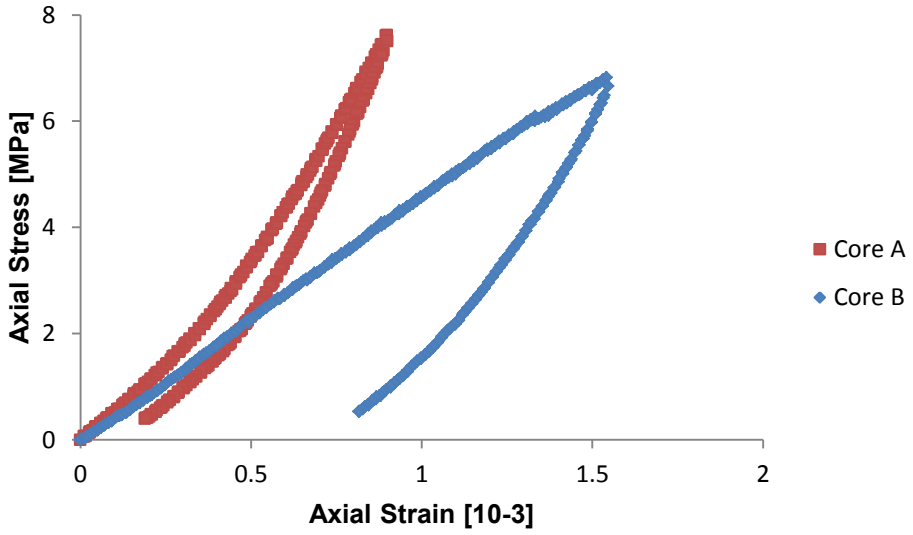

Figure 2.4: Comparison of loading-unloading stress-strain curves for a loading of 10 MPa.

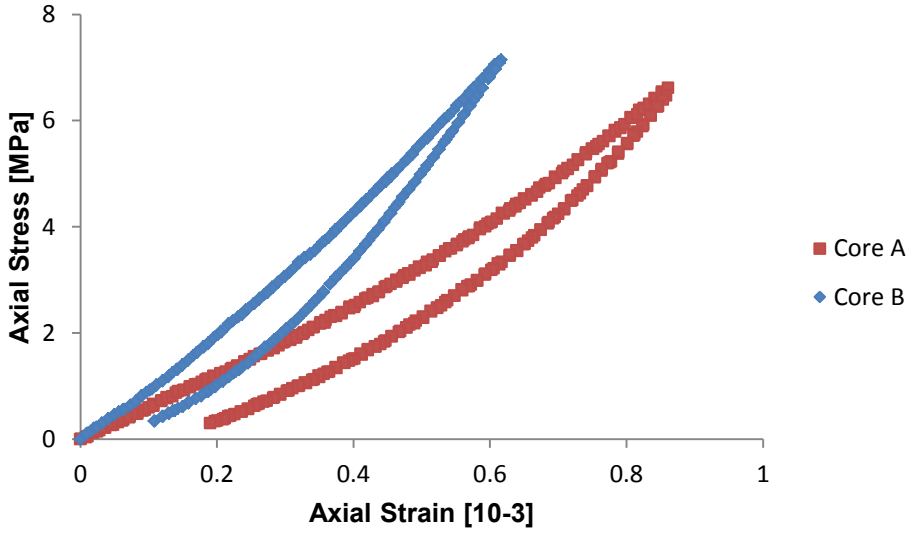

Figure 2.5: Comparison of loading-unloading stress-strain curves for a loading of 12 MPa.

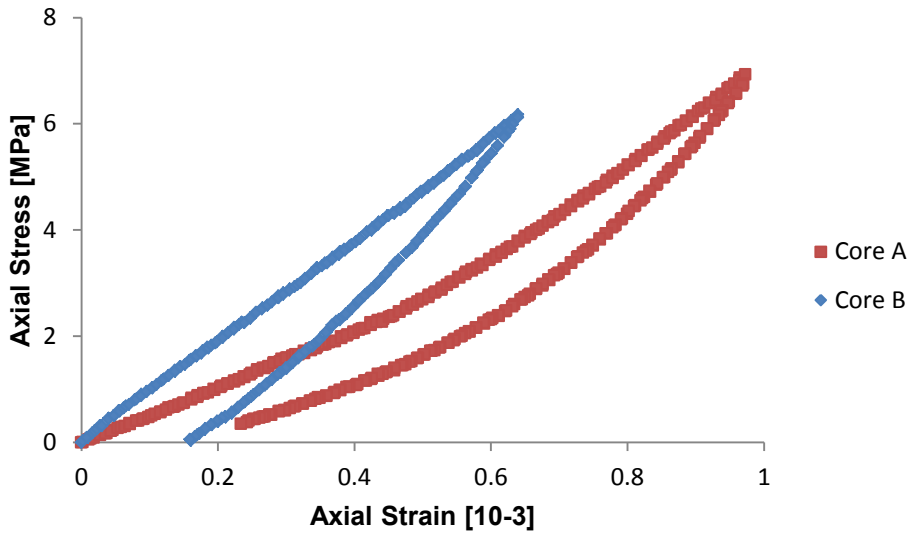

Figure 2.6: Comparison of loading-unloading stress-strain curves for a loading of 14 MPa.

From Table 2.4, it is seen that Young's modulus in loading decreases for 12 and 14 MPa: 13 to 9.17 GPa (30% difference) and 9.78 to 9.11 GPa (7% difference). It can also be observed that Young's modulus in the Core A specimens will decrease as the loading condition increases: 10.60 to 9.17 to 9.11 GPa (10 to 12 to 14 MPa).

Young's modulus in unloading follows a similar trend as the Core A specimens, except for 10 MPa, display lower values: 16.96 to 12.71 GPa (25% difference) for 12 MPa and 15.19 to 13.01 GPa (14% difference) for 14 MPa. Although, the unloading modulus for 14 MPa is higher than 12 MPa.

From the results for crack closure threshold and by viewing the stress-strain curves, it is clear that the stressed cores (Core A) display much more damage than the unstressed cores (Core B). While no trend appears, the crack closure threshold is around 5 – 6 MPa for the Core A specimens while it seems almost non-existent for the Core B specimens. The 12 MPa Core B specimen does display a threshold of above 5 MPa, but Figure 2.5 clearly shows the curvature being much less than the Core A specimen.

The energy loss from hysteresis matches well with the change in behavior of Young's modulus. Besides the 10 MPa Core B specimen, the energy loss increases for 12 and 14

MPa: 0.425 to 0.655 J/m^3 (54% difference) and 0.639 to 0.804 J/m^3 (25% difference). The energy loss from hysteresis also increases with loading condition: 0.634 to 0.655 to 0.804 J/m^3.

Except for the Core B specimen for 10 MPa, there is a clear sign of damage when comparing Young's modulus, crack closure threshold, and energy loss from hysteresis. If the cores were loaded in uniaxial tension, it would be expected that the effect of double elasticity would be more pronounced in the Core A specimens [29] and the tensile strength would be lowered.

Since many methods of determining the in-situ stress state depend on the elastic and strength parameters of the rock, laboratory tests on cores may be misrepresentative if those values are applied to the rock mass. The stress magnitude that causes noticeable damage along with the influence of this damage on elastic and strength properties remains unknown. Yet, the fact that excavating in stressed mediums produce damaged cores should be recognized as an important factor when attempting to measure the *in-situ* stress states.

Chapter 3: Elastic Analysis and Plasticity Concepts

3.1 Numerical Setup

Simulations of core disking was performed with FLAC v. 7.0 [30], a two dimensional finite difference code that is capable of modeling non-linear problems. A wide range of elasto-plastic constitutive models are available, including strain hardening/softening, which is used to simulate core disking.

3.1.1 Grid Generation

Because the particular core disking situation is analyzed with equal horizontal stresses, the problem is axisymmetric. In a cylindrical coordinates system (r,θ,z), tangential strain (ε_θ) always remains zero, allowing three dimensional problems to be simplified into two dimensions.

The entire mesh was split into three separate grids: the core, excavation path, and external boundaries. The height and radial lengths of all three was set to the physical dimensions of the experiments. Element shape has been shown to influence results, so square elements were implemented in the core to minimize any mesh dependency [31]. The vertical height of elements in the excavation path is equal to those in the core, but due to the non-integer ratio between the core radius and radial length of the bit (excavation path), the radial lengths of elements differ. To increase computing speed, elements in the external boundary are larger than those in the core and excavation path. The *ratio* feature was used to prevent large element size differences when transitioning from the core or excavation path to the external boundary. This creates highly rectangular elements near the external boundaries, which usually should be avoided, but can be justified with the low stress and strain gradients in the region. To increase model efficiency, the *attach* command was used to connect elements in the core and excavation path to the external boundary in situations where elements in the core and excavation path are very small. This allows larger elements, by a length factor of two, to be used in the external boundaries, reducing elements and runtime.

Figure 3.1 displays the mesh replicating the Calcarenite disking experiment. The core radius is 16 mm, radial bit length is 3 mm, and overall radius is 80 mm. The height of the core and excavation path was set to 106.25 mm since excavation would not occur throughout the core, but would stop around midheight. The black crosses represent locations where the *attach* command was used.

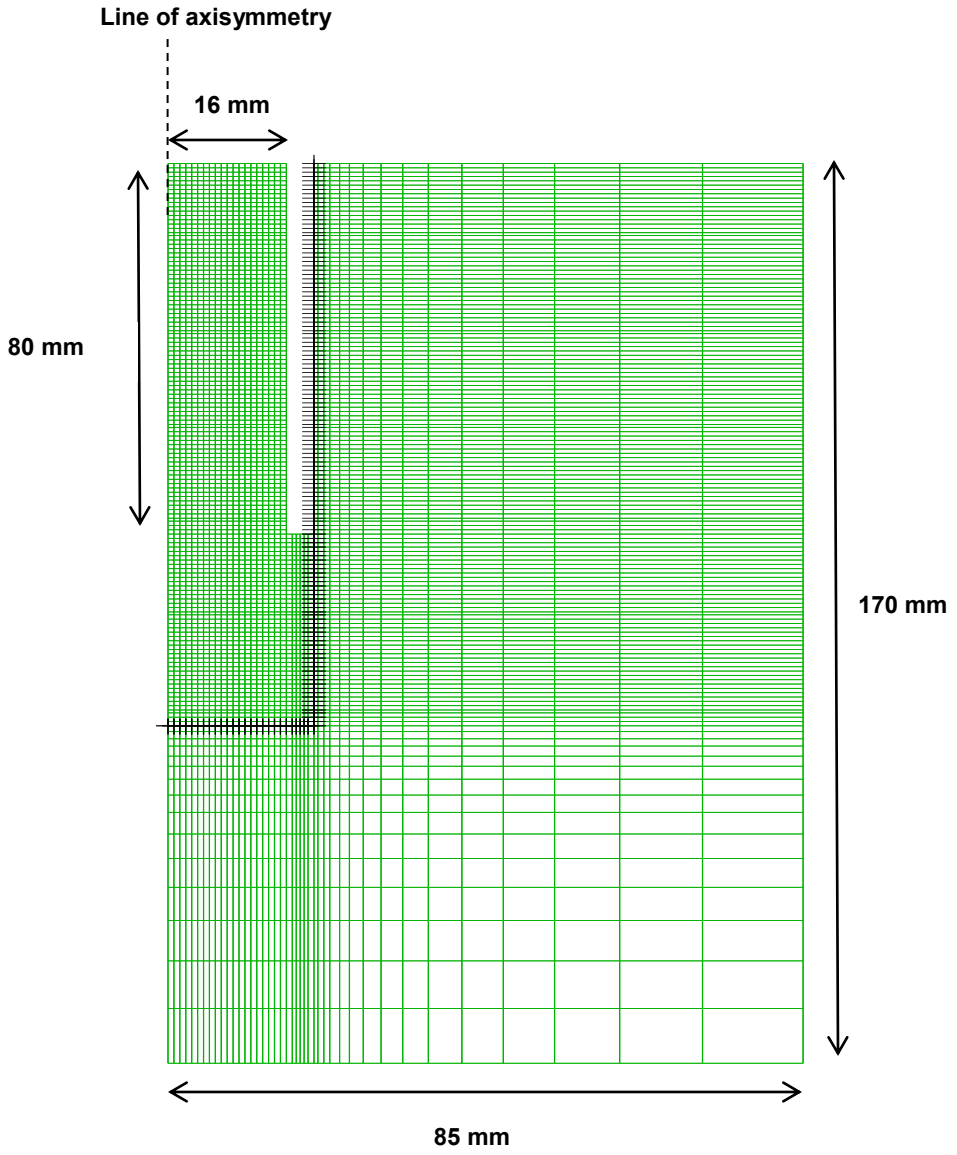

Figure 3.1: Mesh representing an excavated Calcaronite specimen. Note: dimensions and notes will be filled in later.

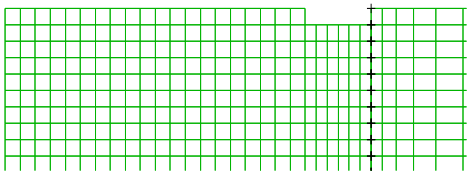

Figure 3.2: Diagram of first excavation step.

Since disking was not experimentally observed for Calcarenite, a detailed numerical analysis was not performed, but the preliminary simulations are shown in Section 4.7. Instead, the majority of the analysis simulates Georgia granite, a rock used by Obert and Stephenson. Different element sizes are required for both materials, since the element size was determined as twice the grain size, which is recommended for mode I fracture situations in continuum models [31]. The grain size for Calcarenite (0.25 mm) is much smaller than then the granite (1 mm), so the element sizes for Calcarenite will be four times smaller as well.

3.1.2 Boundary Conditions

Boundary conditions play an important role in stress analysis and can have large effects on the outcome of numerical simulations. Two different boundary conditions can be implemented: stress and displacement controlled. “Stress” boundaries involve applying traction to the external grid points on the radial boundary. This allows the external boundary to displace and simulates a flexible boundary condition. Displacement boundaries involve fixing radial velocities while initially setting the stress tensor within each element. This inhibits boundary displacement and simulates a rigid boundary condition. If an infinite boundary condition is needed, in field simulations for example, it has been shown that the stress and displacement boundary conditions tend to bound analytical solutions [30]. The boundary conditions used in the analyses are stress controlled.

Since the applied vertical stress equals zero, the vertical boundary conditions are not of extreme importance. The bottom boundary was fixed against vertical displacements. This condition affects only the displacement field, not the stress or strain distributions.

To simplify the problem, only mechanical effects from material removal were considered. Bit pressure, fluid pressure, thermal effects, and saturation may potentially influence disking, but those factors were not included.

3.1.3 Excavation Process

To simulate the coring process, a single row of elements in the excavation path are nulled and the model is allowed to reach equilibrium. The process was repeated until the desired excavation depth was reached. The null constitutive model eliminates the element by setting all material, grid, and grid point properties to zero.

3.2 Numerical Results

A closed-form analytical solution does not exist for the elastic distribution in an attached core. Previous researchers have conducted in-depth axisymmetric and three-dimensional linear elastic analyses, but grid density, boundary conditions, and Poisson's ratio can play a significant role, so it is important to check with previous work. A radial (lateral) stress of 1 MPa, for ease of normalization, was applied to the grid since the experiment only requires lateral stresses. Consensus exists that disking occurs from a tensile failure mechanism so only the minor principal stress (σ_3) is examined.

Standard rock mechanics sign convention, compression positive, is followed throughout the thesis but in this section (3.2 Numerical Results), the absolute value of all results were taken to prevent confusion from sign convention. If the absolute value was not taken, the tensile stress normalized by a compressive radial stress will result in a negative number.

3.2.1 Elastic Analysis

Agreeing with previous work, the elastic stress distribution continuously changes as the excavation proceeds [6,8]. To organize the stress distribution response, three "stages" were identified. Each stage represents similar behavior that occurs over a particular range of excavation depths (z). Figure 3.3 shows the minor principal stress contours (tension only) for three select excavation depths, one from each stage.

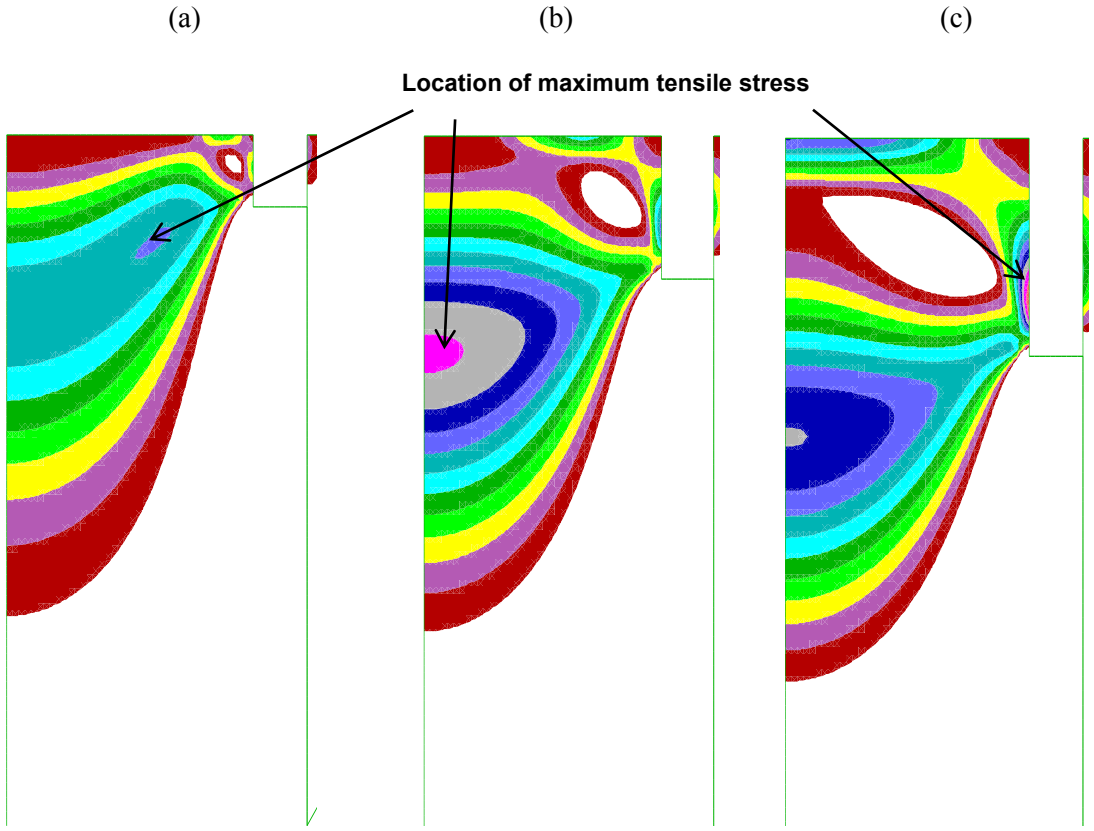

Figure 3.3: Minor principal stress contours (tension only) when excavation depth is (a) 25% R (stage one), (b) 50% R (stage two), and (c) 75% R (stage three).

Initially, in the first stage after a single row of elements in the excavation path have been removed (z = 2.5% R), a tensile stress region forms near, but not along, the core boundary. As the excavation proceeds, this region (tensile region one) moves towards the core center, while also increasing in depth and magnitude. The excavation depths where this behavior occurs, identified as stage one, is from 0 – 30% R. The minor

principal stress distribution, where colored regions are tension, can be seen in Figure 3.3a.

As the excavation proceeds, tensile region one location reaches the core center, where it remains for the remainder of the excavation. The depth of the maximum tensile stress stays below the excavation depth and the tensile stress magnitude reaches a peak value, a magnitude around 25.5% of the radial stress, and then decreases. This behavior is identified as occurring in stage two (z = 30 - 60% R) and can be referenced in Figure 3.3b.

While in stage two, a second tensile stress region develops along the core boundary. This second region is located above the excavation path, with a stress magnitude smaller than in stress region one. As the excavation proceeds, this second stress region along the core boundary eventually produces higher stress magnitudes than the first stress region in the core center (Figure 3.3c). The tensile stress magnitude continues to increase until reaching a steady state condition with a stress value dependent on the grid density. Finer grid densities produce higher stress values due to the extremely large stress gradient. This will be referred to as stage three. These results match well with Stacey [6] and Li and Schmitt [8].

From previous elastic and elasto-plastic analyses, disagreement over the location of tensile fracture initiation still exists. Some researchers argue for the core center [9,10,23], some say the core boundary [11,14], and others claim either, depending on the "stage" [6,8]. Because of this uncertainty, the element experiencing the largest tensile stress magnitude in the entire core, core center, and core boundary were located and recorded at each excavation cycle. For example, after a single excavation cycle (one row of elements removed in the excavation path), all elements in the "future" core were checked and the largest tensile stress (smallest minor principal stress assuming compressive positive notation) was recorded (blue diamond data points). The columns of elements along the line of axisymmetry (Core Center – green triangle data points) and core boundary (Core Boundary – red square data points) were also checked. If the

largest tensile stress is located at the core center (Stage Two) or core boundary (Core Center), the blue diamond data points will overlap the green triangle or red square data points. Figure 3.4 shows the evolution.

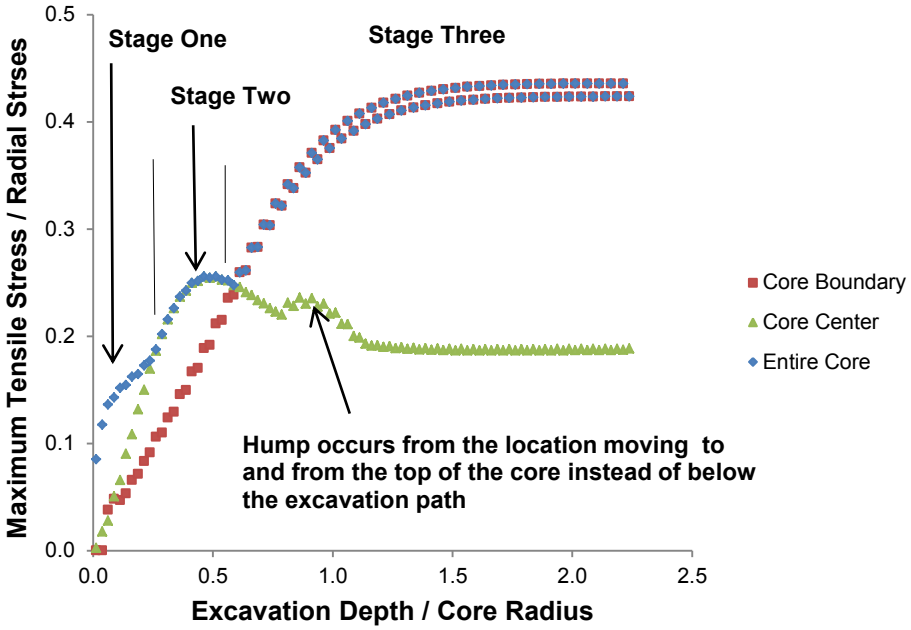

Figure 3.4: Progression of maximum tensile stress, normalized by radial stress, in the entire core, core center, and core boundary as the excavation proceeds

As both Figures 3.3 and 3.4 show, the largest tensile stress throughout the entire core (blue diamond data points) follows an irregular, highly non-linear relation as the excavation proceeds. The two specified radial lengths, core center (green triangles) and core boundary (red squares), provide an explanation for the complex relation as it appears that quick shifts in the relation are often due to the largest tensile stress switching locations. It can be further observed that relations at particular radial distances, core center or core boundary, are actually smooth and continuous. It also identifies the three stages and predicts that disking could potentially occur from multiple locations in the core. It should be noted that stresses along the core boundary tend to fluctuate as the excavation proceeds. This is not a failure to reach static equilibrium but most likely due to the extremely high stress gradient in the region.

3.2.2. Elastic Analysis with Strength Limits

Since only disk thickness is observed in the field, an elastic disking criterion was examined to relate the radial stress to the disk thickness. Disking is hypothesized to result from a tensile failure mechanism, so it was assumed that a fracture will initiate and propagate at the depth of the first element to satisfy the tensile strength limit. To implement this, the largest tensile stress magnitude at each excavation cycle (σ_t/σ_R vs z/R), seen in Figure 3.4, was combined with the depth of the element experiencing the largest tensile stress (t/R vs z/R) at each excavation cycle. The criterion can be seen in Figure 3.5, with the blue diamond data points being compared with the best fit data results from Lim and Martin for Lac du Bonnet granite and granodiorite at the URL Tunnel in Canada [22].

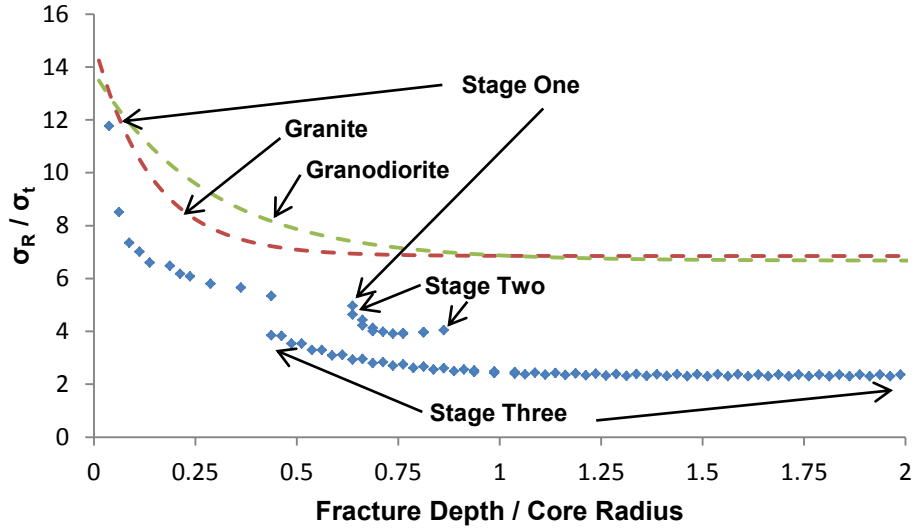

Figure 3.5: Maximum (radial) stress normalized by tensile strength versus fracture depth (disk thickness) normalized by core radius for simulation data and best fit data from Lim and Martin [22].

From the plot, it can be seen that the disking relation is different for all three stages. Stage one has a smooth relation but the required radial stress to initiate disking drops while entering stage two. A jump in fracture depth occurs while transitioning into stage

three, due to the region of maximum tensile stress switching locations, and then extends at a steady disking initiation stress.

When comparing the results with field data from Lim and Martin [22], it can be seen that the relation in stage one matches field studies to a reasonable degree but underestimates the maximum principal stress. Stages two and three do not match as well, but it would be difficult to observe physically due to the large scatter of results in field and laboratory studies.

This underestimation is not surprising because the assumption that fracture occurs when the tensile strength is reached does not hold for quasi-brittle materials. Instead, a softening relation should be used. Yet, Figure 3.5 can be referenced as a "yielding criterion" for core excavations and it verifies that, assuming fracture occurs in stage one, the curve matches with field results.

To predict the probable fracture orientation at each excavation stage, the angle of the major principal stress was determined since it dictates the direction of fracture. In region one, the angles reached -10°, positive convention being counter-clockwise from horizontal, but remained around 0 - 2° in region two and three. This suggests all disking in axisymmetric conditions will be flat or dictated by heterogeneity in the rock. This matches field and laboratory results [5,11,21,22]. While predicting the fracture orientation is not imperative for flat disking, it may prove to be useful when simulating core disking in unequal horizontal stress states where the fracture may not be flat.

3.2.3 Grid Density

To determine the effect on the elastic stress distribution, four different grid densities were used. In the first grid density scenario (GD1), the height and width of the elements in the core were 0.1 R x 0.1 R (1.6 mm x 1.6 mm). The second (GD2) was 0.05 R x 0.05 R. The third (GD3) was 0.033 R x 0.033 R and 0.025 R x 0.025 R (0.4 mm x 0.4 mm) for GD4. Note that GD4 was used in the previous section and for Calcarenite,

while GD1 is used for Georgia granite. Figure 3.6 shows the maximum tensile stress for each excavation stage for all four grid densities.

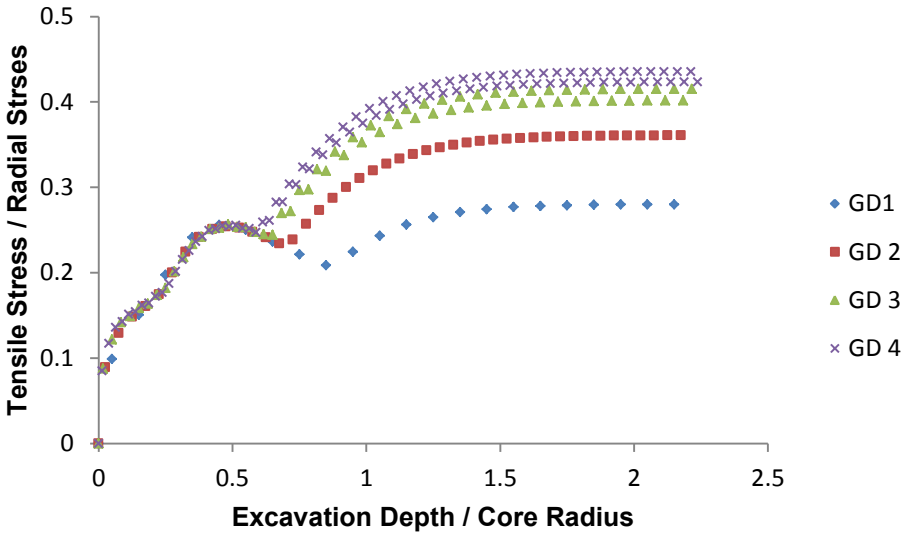

Figure 3.6: The influence of grid density on maximum tensile stress during excavation.

As can be seen, GD1 is a sufficient grid density when the maximum tensile stress is located in stages one and two due to a lack of high stress gradients. Once the maximum tensile stress moves to stage three, the extremely high stress gradient requires very fine grid densities since the maximum tensile stress increases as the grid becomes denser.

3.3 Plasticity Concepts

3.3.1 Failure Criteria

First, the modified Mohr-Coulomb (MC) failure criterion with a strain softening constitutive relation was used [32]. While the yield surface for frictional materials is non-linear, the modified Mohr-Coulomb failure criterion simplifies the behavior with a linear yield surface. This has proved to be effective as long as a small variation of σ_3 is being analyzed. In FLAC, the modified Mohr-Coulomb constitutive relation consists of

two independent failure modes: shear and tension. The shear failure mode is defined by the Mohr-Coulomb yield surface [30]:

$$f_s = \sigma_1 - \sigma_3 N_\varphi - 2c\sqrt{N_\varphi} \tag{3.1}$$

$$N_\varphi = \frac{1 + \sin(\varphi)}{1 - \sin(\varphi)} \tag{3.2}$$

where c is cohesion, and σ_1 and σ_3 are the major and minor principal stresses. The tensile failure mode is defined by the Tension Cutoff yield surface:

$$f_t = \sigma_t - \sigma_3 \tag{3.3}$$

where σ_t is the uniaxial tensile strength. Yielding occurs when either f_s or f_t equals zero. Figure 3.7 shows a typical MC failure criterion with both yield surfaces.

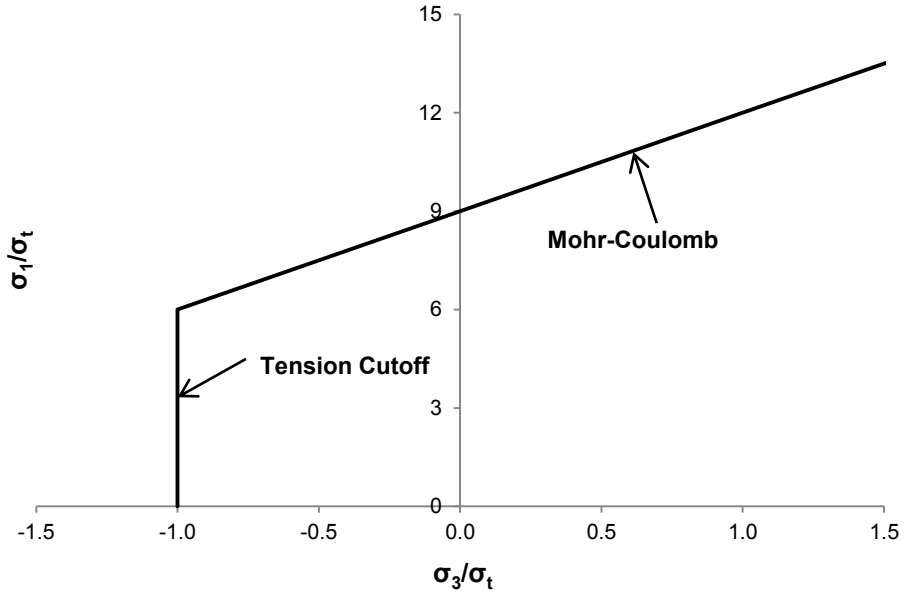

Figure 3.7: Modified Mohr-Coulomb failure criterion including both a Mohr-Coulomb yield surface, functions of cohesion (c), and friction angle (ϕ) and tension cutoff yield surface, a function of tensile strength (σ_t).

When yielding occurs, a flow rule, non-associated for shear and associated with tension, is used to determine the plastic strains. The flow rule for the shear failure mode has the following form:

$$\Delta e^p = \lambda^s \frac{\partial g^s}{\partial \sigma} \tag{3.4}$$

where g^s is the shear potential function: $g^s = \sigma_1 - \sigma_3 N_\psi$

$$N_\psi = \frac{1 + \sin(\psi)}{1 - \sin(\psi)} \tag{3.5}$$

where λ_s is a scalar multiplier, and ψ is the dilation angle. The flow rule for the tensile failure mode has the following form:

$$\Delta e^p = \lambda^t \frac{\partial g^t}{\partial \sigma} \tag{3.6}$$

$$g^t = -\sigma_3 \tag{3.7}$$

An alternative yield condition is the Hoek-Brown (HB) criterion, a non-linear yield surface that attempts to capture the behavior of cohesive frictional material. The failure criterion has been proven effective at analyzing a wide range of stress states when the linear simplification of modified Mohr-Coulomb was considered insufficient. The yield equation is [33]:

$$F = \sigma_1 - \sigma_3 - \sigma_{ci}\left(m_b \frac{\sigma_3}{\sigma_{ci}} + s\right)^a \tag{3.8}$$

where m_b is a reduced value of material constant m_i and s and a are constants for the rock mass dependent on the geological strength index (GSI) and disturbance factor (D). For intact rock, GSI = 100 and D = 0, giving $m_b = m_i$, s = 1, and a = 0.5. The uniaxial tension strength under uniform tension for intact rock can be defined as:

$$\sigma_t = -\frac{\sigma_{ci}}{m_b} \tag{3.9}$$

Although the tensile strength under uniform tensile and uniaxial tensile strength is assumed to be equal [33], if m_b values are low, the Hoek-Brown failure criterion produces different values. If m_b values are low, the following equation gives the uniaxial tensile strength:

$$\sigma_t - (m_b\sigma_{ci})\sigma_t - (\sigma_{ci})^2 = 0 \tag{3.10}$$

An example of the yield surface for Hoek-Brown, compared with modified Mohr-Coulomb, is shown in Figure 3.8.

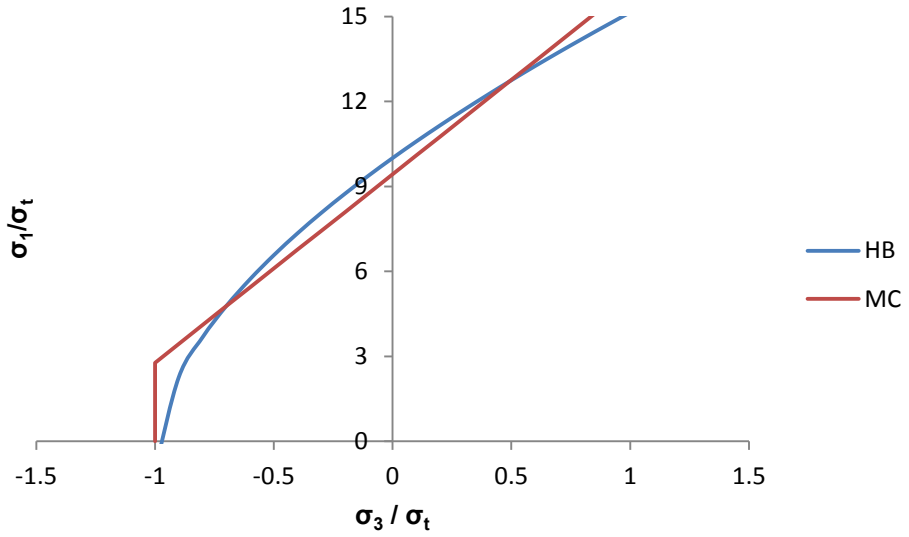

Figure 3.8: Hoek-Brown yield surface compared with an equivalent modified Mohr-Coulomb yield surface.

To analyze the post-yield behavior of materials using the Hoek-Brown failure criterion, Cundall et al. applied different flow rules to empirically match observed failure modes [34]. From the elastic analysis, all core disking failure should occur in situations where the major principal stress is compressive and the minor principal stress is either tensile, zero, or experiencing low levels of compression. An associated flow rule for $\sigma_3 \leq 0$ and composite flow rule for $0 \leq \sigma_3 \leq \sigma_3^{cv}$ are used, where σ_3^{cv} is the confining stress where dilation no longer occurs. The flow rule relating the major and minor principal plastic strain magnitudes is:

$$\Delta e_1^p = \gamma \Delta e_3^p \tag{3.11}$$

where γ depends on the type of flow rule. The associated flow rule ($\sigma_3 \leq 0$) can be defined:

$$\Delta e_i^p = -\gamma \frac{\partial F}{\partial \sigma_i} \tag{3.12}$$

When differentiated, the following equation results:

$$\gamma_{af} = -\frac{1}{1 + a\, m_b \left(m_b \frac{\sigma_3}{\sigma_{ci}} + s \right)^{a-1}} \tag{3.13}$$

The composite flow rule ($0 \leq \sigma_3 \leq \sigma_3^{cv}$) is an interpolation between the associated flow rule and constant-volume flow rule, which applies when $\sigma_3^{cv} \leq \sigma_3$. The constant volume flow is defined as:

$$\gamma_{cv} = -1 \tag{3.14}$$

The composite flow rule the can be represented as:

$$\gamma = \frac{1}{\frac{1}{\gamma_{af}} + \left(\frac{1}{\gamma_{cv}} - \frac{1}{\gamma_{af}}\right)\frac{\sigma_3}{\sigma_3^{cv}}} \tag{3.15}$$

These flow rules allow a wide possibility of fracture orientations [34], instead of the two associated (shear band or tensile fracture) with modified Mohr-Coulomb.

3.3.2 Softening and Fracture

To simulate a fracture with the modified Mohr-Coulomb failure criterion, a smear cracking approach is taken. Smear cracking assumes an infinite number of cracks with infinitely small openings are smeared over a finite element, which can replicate the fracture process in a continuum code [31]. To model this, the element's strength is gradually reduced – called strain softening - as a function of plastic strain. This

approach was selected since the location of fracture is unknown while the orientation is known to be horizontal, allowing the fracture to propagate along a row of elements. In more complex analyses, where the fracture orientation will not be horizontal, other approaches can be taken and these are addressed later in the thesis.

The tensile strain softening relation can be constructed from the fracture energy of the material by first assuming the relation to be linear. Then, by integrating the relation, the fracture energy density can be defined:

$$\gamma_F = \int_0^{\infty} \varphi(\varepsilon^f) d\varepsilon^f = \frac{\sigma_t * S_p}{2} \tag{3.16}$$

where γ_F is the fracture energy density, ϕ is the softening relation, σ_t is the peak tensile strength, and S_p is the plastic strain of the element at fracture. Figure 3.9 shows the relation.

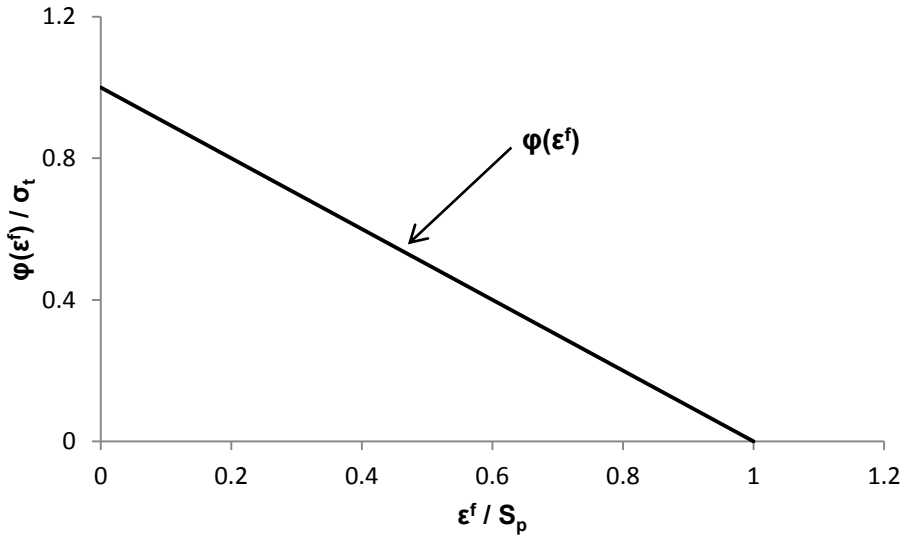

Figure 3.9: Softening relation between tensile strength and plastic tensile strain.

The fracture energy density can be multiplied by the height of the element (h_c) to get the fracture energy.

$$G_f = \frac{1}{2} h_c \sigma_t S_p \tag{3.17}$$

and the plastic tensile strain (S_p) at failure is given by:

$$S_p = \frac{2G_f}{h_c \sigma_t} \tag{3.18}$$

If multiple element heights are to be used, S_p must be updated as well. This update of S_p is an aspect of the Crack Band Model and should be used to minimize numerical scaling effects during tensile fracture simulations [31].

Since FLAC is a continuum code, the element will remain even if the tensile strength is reduced to zero, simulating a "fracture." This allows the element to still experience compressive and shear stresses, since shear and tensile failure modes are independent in the modified Mohr-Coulomb failure criterion, which can affect the fracture depths later in the simulation. To avoid these effects and reduce computation time due to the excessive plastic strains that occur after "fracture," elements experiencing a tensile strength of zero were nulled, creating a discontinuous surface.

To simulate fracture with the Hoek-Brown failure criterion, a smear cracking approach was again taken with the fracture energy calculated in a similar fashion. The Hoek-Brown failure criterion only has a single yield function, F, which is dependent on the uniaxial compressive strength, σ_{ci}, and material constant, m_b. Since the reduction of m_b will result in a non-linear tensile softening response, the uniaxial compressive strength will be reduced to zero, as a function of plastic strain, once yielding has occurred. Physically this is not realistic, but without a separate tensile failure mode in the Hoek-Brown model, either σ_{ci} or m_b must be reduced.

One constraint that appears when using a smear cracking approach is minimum element size, also defined as the crack band width. It has been shown that the element size should be roughly 2-5 d_a, where d_a is the maximum grain size when simulating fracture [31]. If an element size is smaller than the grain size, any numerical result is considered meaningless from a physical standpoint. While this usually does not present an issue when simulating most fracture tests due to the large specimen to grain size ratio, core disking can produce disks with thicknesses around the grain size. With such large

element sizes, it can limit the potential range of analysis and cause uncertainties that the grid density may not be fine enough.

An important parameter in fracture and scaling analyses is the characteristic length. This material property allows length scales to be normalized by a material property and not an external condition such as core radius. The equation defining characteristic length for Mode I fracture is:

$$\ell_{ch} = \frac{G_f E}{{\sigma_t}^2} \tag{3.19}$$

Physically, the characteristic length is related to the length of the fracture process zone (FPZ), the damaged area ahead of the crack. The FPZ is responsible for the scaling effect observed in rock and other quasi-brittle materials [31].

CHAPTER 4: Numerical Simulation

4.1 Mohr-Coulomb (MC) Failure Criterion

Due to the complexity of rock failure, it is important to choose an appropriate model that simulates the failure process for the particular situation. In previous attempts to numerically simulate disking, multiple models were used by different researchers and it remains unclear which best represented the failure process [11-16]. While disking has been replicated for lower stress levels, a shear failure mode controlled failure at higher stresses [13,15], which has not been observed in field studies. Therefore, it is imperative to select a model that can simulate the failure process for a wide range of stresses.

To determine an appropriate model, simulations of Georgia granite, using various failure criteria and constitutive models, are compared to the experimental results from Obert and Stephenson [5] and field disking trends from Lim and Martin [22]. Corthésy and Leite numerically replicated the laboratory results of Obert and Stephenson with FLAC using a cohesion softening friction hardening model [13] and their work is used as a starting point for this analysis. The preliminary results from Calcarenite are also displayed in Section 4.6. The strength properties for Calcarenite and Georgia granite are presented in Table 4.1.

Table 4.1: Material properties of Georgia granite and Calcarenite [5,28]

Material	**Young's modulus**	**Poisson's ratio**	**Uniaxial compressive strength**	**Cohesion**	**Friction angle**	**Tensile strength**
	[GPa]	**[-]**	**[MPa]**	**[MPa]**	**[°]**	**[MPa]**
Calcarenite	8.35	0.237	16.1	5.62	22.0	2.5
Georgia granite	26.0	0.35	153.3	26.4	52.0	9.1

For simulations on Georgia granite, a core radius of 24 mm was used and a radial stress of 7.7 σ_t (70 MPa) was applied. From the results from Obert and Stephenson (1965), the following disking initiation stress equation was proposed [5]:

$$S_r = k_1 + k_2 S_a \quad (4.1)$$

where S_r = applied radial stress in psi, S_a = applied axial stress in psi, k_1 = S_r axis intercept, and k_2 = slope of the least square line. Since the numerical simulation assumes S_a equals zero, the S_r will equal k_1, which is defined as:

$$k_1 = 3400 + 2.0c \quad (4.2)$$

where 3400 is in psi and c is cohesion in psi. The cohesion of Georgia in granite is 3,300 psi, producing a k_1 value of 10,000 psi, or around 68.9 MPa (7.7 σ_t). Therefore, from this empirical relation, disking should not occur at values below 65 MPa (7.14 σ_t), but since no test was performed at that stress magnitude, it will be assumed that disking should not occur below 60 MPa (6.6 σ_t). From the photographs, disk thicknesses were around 35% of the core radius [5]. The experimental results of Georgia granite were used to verify the numerical models.

Five different models were tested. The first three used the modified Mohr-Coulomb (MC) failure criterion while the latter two used the Hoek-Brown (HB) failure criterion. The constitutive models using the MC failure criterion were cohesive softening (CS), cohesive softening friction hardening (CSFH), and tensile softening (TS). The models using HB failure criteria were a HB equivalent of the CS and TS models. Details of all the models will be explained in the next few sections.

4.1.1 Cohesive Softening (CS)

Since softening parameters are required for disking, the simplest model is a cohesive softening (CS) tensile softening relation. In this model, only cohesion and tensile strength are treated as functions of accumulated plastic strain. Once yielding occurs, the values of cohesion and tensile strength will drop to zero after a specified residual strain has been reached and linear interpolation determines the strength between specified

plastic strain values. The softening parameters and strength values used are shown in Table 4.2.

Table 4.2: Table displaying the softening values of cohesion, friction angle, tensile strength, and dilation angle as functions of plastic strain for both Calcarenite and Georgia granite [23].

Plastic strain	**Cohesion**	**Friction angle**	**Tensile strength**	**Dilation angle**
[%]	**[MPa]**	**[degree]**	**[MPa]**	**[degree]**
Calcarenite				
0.0	5.62	22.0	2.5	0.0
3.034	0.0	22.0	0.0	0.0
Georgia granite				
0.0	26.4	52.0	9.1	0.0
0.337	15.0	52.0	6.17	0.0
0.472	13.0	52.0	5.00	0.0
0.675	10.0	52.0	4.13	0.0
1.518	2.5	52.0	0.50	0.0
1.687	1.0	52.0	0.0	0.0

Contours of tensile strength (Fig. 4.1a) and cohesion (Fig. 4.1b) values are shown, where gray and teal are the original strength values respectively.

(a) (b)

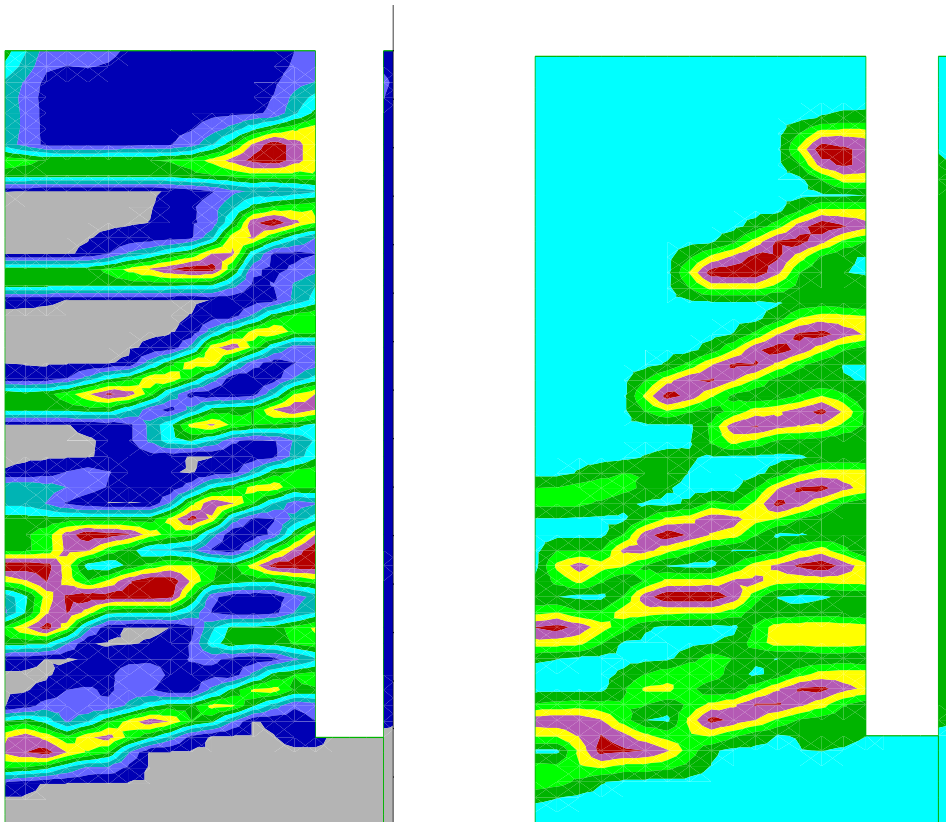

Figure 4.1: Contours of (a) tensile strength and (b) cohesion for CS Model.

The 7.7 σ_t (70 MPa) loading situation will produce a mixed-mode failure, where both yielding in tension and shear occurs. While yielding in tension and shear are considered completely independent in FLAC, a constraint on the tensile strength does exist.

$$\sigma_t \geq \frac{c}{\tan(\varphi)} \tag{4.3}$$

This is represented as the minor principal stress value where the Mohr-Coulomb yield surface touches the hydrostatic axis (Figure 4.2).

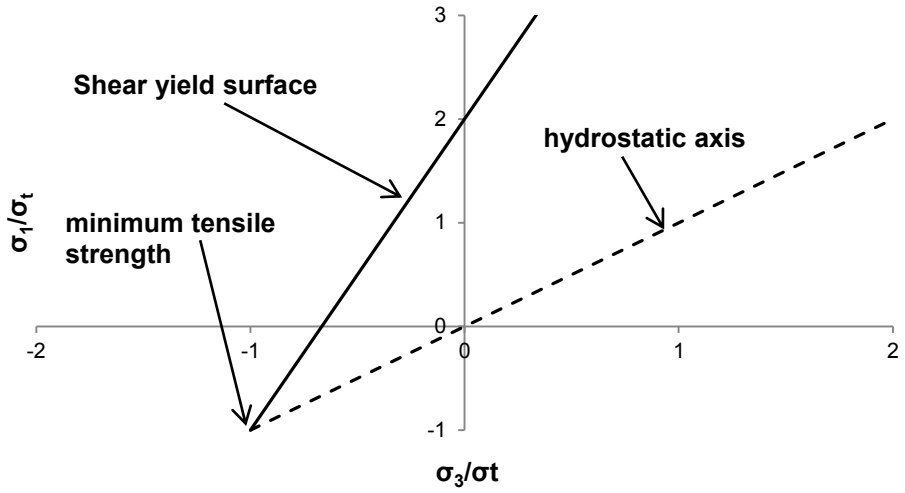

Figure 4.2: Mohr-Coulomb yield surface showing minimum tensile strength value (compression positive).

Tensile strength values lower than this value (compression positive) are meaningless so the relation is enforced. Therefore, if significant cohesion softening occurs, tension softens as well. This explains the angled bands in tension (Fig 4.1a) following the angled shear bands (Fig 4.1b). The mixed-mode failure can be explained by following the stress paths (Fig 4.3) of elements that failed in tension (horizontal bands) or shear (angled bands).

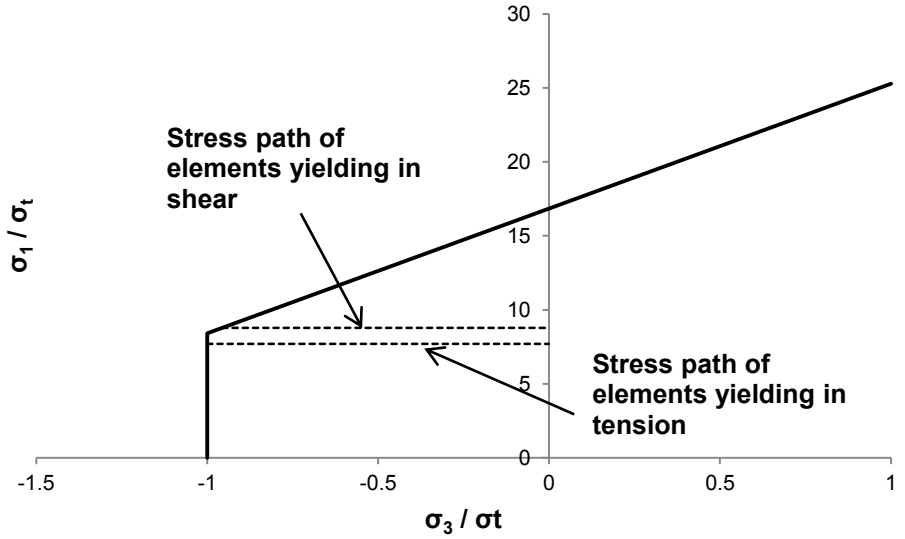

Figure 4.3: Stress path of elements yielding in shear in tension for CS model.

Since mixed-mode failures were not observed by Obert and Stephenson [5], and have not been observed in core disking situations, this suggest the standard yield surface for Mohr-Coulomb is not appropriate and other models should be used.

4.1.2 Cohesive Softening Friction Hardening (CS FH)

One potential issue that arises with continuum numerical models, especially when using the Mohr-Coulomb failure criterion, is simulating failure in low confined regions. When modeling a uniaxial compression test in FLAC using the Mohr-Coulomb failure criterion, the strength limit is set by a combination of the friction angle and cohesion.

$$C_o = \frac{2c}{\tan(45 + \frac{\varphi}{2})} = \frac{2c * \cos(\varphi)}{1 - \sin(\varphi)} \tag{4.4}$$

The failure plane, according to bifurcation theory, should be oriented at a particular angle from the major principal (horizontal) plane, depending on the friction and dilation angle [35,36].

$$\beta = 45 + \frac{1}{4}(\varphi + \psi) \tag{4.5}$$

While the numerical model can precisely follow the yield condition, physical experiments show an axial splitting failure mode, not a shear (Mohr-Coulomb) failure mode. Axial splitting will not be replicated in the numerical model. Another example is given by the recent attempts to numerically replicate spalling failure in brittle rock. It has been proposed to incorporate an S-shaped failure criterion in regions of low confinement [37-40]. A third example is the use of a cohesive softening friction hardening (CS FH) model to replicate V-shape notch found in tunnel excavations experiencing certain stress conditions [41-43]. The CS FH model states that cohesion and friction can mobilize at different rates depending on the situation, potentially giving different strength values in the field than what was observed in laboratory conditions [44].

These three examples show situations where MC theory may not be an appropriate model for analysis. Since core disking involves failure in the tensile/lowly confined region, it is plausible that shear failure will not occur as the CS model predicts and an alternative model that promotes tensile failure should be used.

Corthésy and Leite suggested using a CS FH model. In their simulations, the initial friction angle was reduced to 13° from 52° and cohesion was raised to 61.0 MPa from 26.4 MPa to keep the uniaxial compressive strength constant. After yielding occurred in shear, friction would mobilize after a plastic strain of 0.01 while 0.05 is needed for cohesion to reach its residual value. This model was successful in capturing the disking effect and thickness for Georgia granite to an acceptable degree. When simulating the problem with larger radial stresses than what was tested by Obert and Stephenson, shear failures dominated in the same fashion as in the CS model. The result from the simulation is shown in Figure 4.4.

(a) (b)

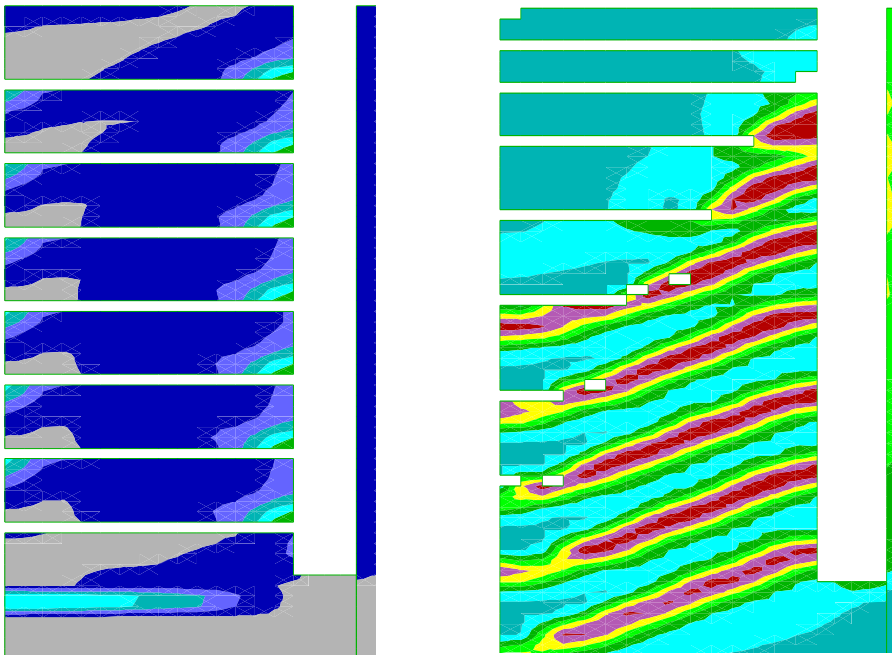

Figure 4.4: Contours of tensile strength in Georgia granite (a) for an applied stress of 7.7 σ_t (70 MPa) (a) and contours of cohesion in Georgia granite (b) for an applied stress of 13.2 σ_t (120 MPa).

The average disk thickness is higher than expected: 46.7% of the core radius. While this is different from the 35% found by Obert and Stephenson, each element is 6.7% of the core radius and is only one element difference from the 39% reported by Corthésy and Leite [13].

The reason the CS FH (and not CS) model was able to capture the disking is due to the difference in yield surfaces. In the principal stress plane, shown in Figure 4.5, the tensile and uniaxial compressive strengths are the same. The higher friction angle in the CS model make the yield surface steeper, meaning the stress path of an element in tension is more likely to touch the Mohr-Coulomb yield surface than in the CS FH model. Therefore, the CS FH model was able to promote tensile failure in the core, producing disking in situations where it was not observed in the CS model. However, as others have noticed [13,15], when the radial stress is increased, the stress paths will eventually touch the Mohr-Coulomb yield surface. This will cause disk thicknesses to increase and eventually a shear failure mode will exist (Figure 4.4b). For this reason, a constitutive model that promotes tensile failure for a wide range of radial stresses should be used.

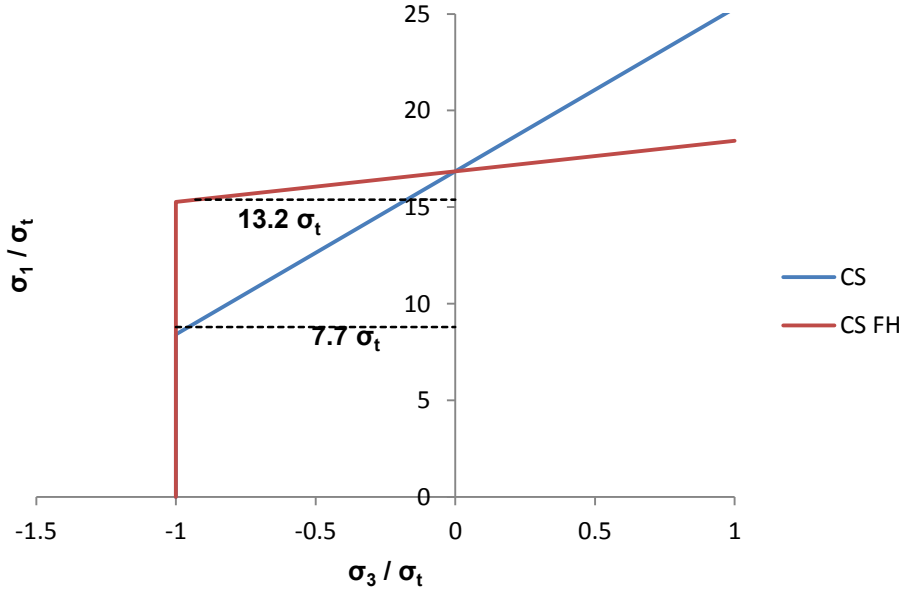

Figure 4.5: Stress paths of elements in for 7.7 σ_t (70 MPa) and 13.2 σ_t (120 MPa) loading situation.

4.1.3 Tensile Softening (TS)

In response to the occurrence of shear failure in the core with the CS FH model, a tensile softening (TS) constitutive model was used. This model eliminates the Mohr-Coulomb yield surface by considerably increasing cohesion, leaving only the tensile cutoff yield surface. It is unrealistic to expect yielding in some form to not occur along the core boundary when the stress state dictates it, but the Mohr-Coulomb failure criterion is not representative in many situations, and core disking seems to be another of these. The formation of microcracks has been used as an explanation for axial splitting and spalling, justifying the use of the CS FH model, so it is possible that microstructural effects have an influence in disking.

While the TC model can promote the disking fractures in the core, yielding does occur in other regions of the model and this yielding can affect the disk thicknesses. For example, the region under the excavation path experiences large stresses and is predicted to yield in shear. This failure mode will not be a disking fracture so therefore there is no need for the TS constitutive model to be applied. In response, the CS model was used outside the core. There is no current evidence suggesting alternative models are needed in those regions.

To verify against experimental results, the post-peak parameters were modified, as shown in Table 4.3. Figure 4.6 displays the tensile strength contours for both 7.7 σ_t (70 MPa) and 6.0 σ_t (55 MPa).

Table 4.3: Post-peak parameters of TS model in the core for Georgia granite.

Plastic strain	**Cohesion**	**Friction angle**	**Tensile strength**	**Dilation angle**
[%]	**[MPa]**	**[degree]**	**[MPa]**	**[degree]**
0.0	260.4	52.0	9.1	0.0
0.506	15.0	52.0	6.17	0.0
0.708	13.0	52.0	5.00	0.0
1.013	10.0	52.0	4.13	0.0
2.277	2.5	52.0	0.50	0.0
2.531	1.0	52.0	0.0	0.0

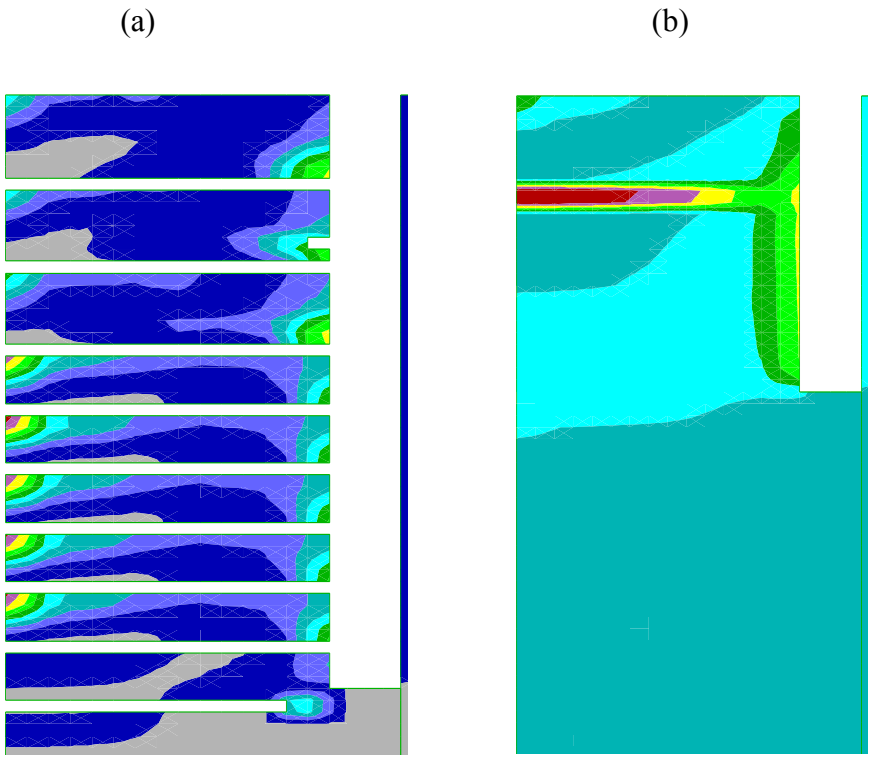

Figure 4.6: Tensile strength contours for (a) 7.7 σ_t (70 MPa) and (b) 6.0 σ_t (55 MPa).

The most common disk thickness for 7.7 σ_t (70 MPa) is 33% the core radius while the average, excluding the first disk, is 36.7%, very close to the experimental results. For the 6.0 σ_t (55 MPa) situation, it can be seen that damage, but no disking, occurs. This matches well with experimental results [5].

4.2 Hoek-Brown (HB) Failure Criterion

Since disking occurs in a stress region where the major principal stress is compressive and the minor is tensile, the modified Mohr-Coulomb failure criterion runs into issues since it is not good at predicting failure around those regions. The Hoek-Brown failure criterion will be used since it attempts to predict yielding in a more realistic manner.

One issue with the HB failure criterion is assigning values. There are equations to convert HB variables into MC form [33] but this often encounters issues since the

modified MC assumes two independent yield surfaces where HB is comprised of only one. To match the MC failure criterion as close as possible, two different HB yield surfaces will be used. The first will attempt to match the CS model and the second will match the TS model. Table 4.4 displays the Hoek-Brown parameters and Figure 4.7 shows the yield surfaces.

Table 4.4: Hoek-Brown parameters of both models assuming intact rock

Model	σ_{ci}	m_b	σ_t	a	s
	[MPa]	[-]	[MPa]	[-]	[-]
HB – CS	153.4	17.0	-9.02	0.5	1.0
HB - TS	1000	110	-9.1	0.5	1.0

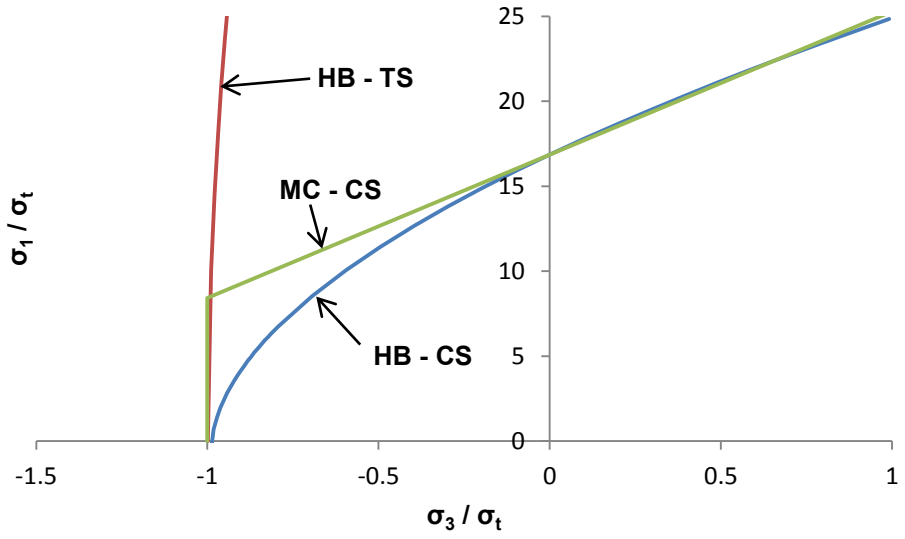

Figure 4.7: Yield surfaces of Mohr-Coulomb cohesive softening (MC-CS) model, Hoek-Brown cohesive softening (HB-CS) model, and Hoek-Brown tensile softening (HB-TS) model.

Applying these yield surfaces and calibrating the softening parameters to match a direct tensile test, the results of both core simulations for 7.7 σ_t (70 MPa) are shown in Figure 4.8.

(a) (b)

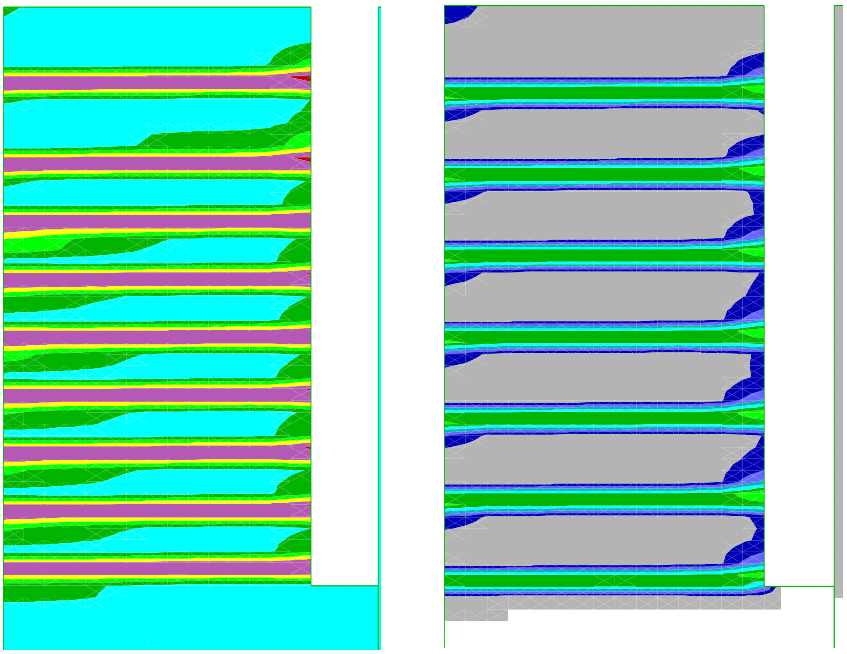

Figure 4.8: Uniaxial compressive strength (σ_{ci}) contours for (a) HB – CS model and (b) HB – TS model.

The Hoek-Brown failure criterion does a good job at predicting disk thickness for both yield surfaces. The HB-CS yield surface predicts disk thickness of 33.0% the core radius while the HB-TS yield surface predicts thicknesses of 46.7% the core radius. However, if the radial stress is increased to 9.9 σ_t (90 MPa), complete failure was observed for both models. This means that every element in the model reaches its residual stress value. This is attributed to the single failure mode in the Hoek-Brown failure criterion, where failure in tension will weaken the rock in shear.

4.3 Failure Process

One aspect of core disking that lacks consensus is the failure process. Since fracture initiation occurs inside the specimen while drilling is proceeding, it is difficult to experimentally determine the behavior and all information must be inferred from analyzing the failed specimen. Numerical models can potentially simulate the behavior,

but each approach (elastic analyses with strength limits, weak plane models, softening models) tends to yield different responses. In addition, various excavation depths and applying vertical and unequal horizontal stresses can significantly change the stress distribution in the core, leading to various possible locations of fracture initiation and propagation. Therefore, it is important to analyze the failure process to understand the underlying conditions that initiate disking fracture.

One of the main difficulties with core disking analyses is the lack of knowledge of the location of fracture initiation. In fracture mechanics, for both crack initiation (Type 1) and crack propagation (Type 2), failure is controlled by a critical stress intensity factor and equations have been developed for many simple Type 2 geometries [31]. Once the stress intensity factor (K_I) reaches a critical value (K_{IC}) the crack propagates. For Type 1 situations, the stress intensity factor is not as obvious but still can be conceptualized due to the formation of microcracks at the future crack tip in a fracture process zone. In a similar manner, when the "stress intensity factor" reaches a critical value, crack initiation occurs. In core disking, this concept, $K_I = K_{IC}$ causes failure, will be used to describe failure for the remainder of the thesis.

To analyze the core disking mechanism and features, Georgia granite will be cored at a radial stress of 7.7 σ_t (70 MPa). This was shown in the previous section to give disk thicknesses of around 36.7% the core radius. The failure process will be analyzed at select excavation cycles.

Similar to the elastic analysis, the excavation process begins by removing a single row of elements from the excavation path and stepping the system to equilibrium (Figure 4.9a). A tensile stress region forms near, but not along the core boundary, with a magnitude that is predicted by the elastic analysis (0.1 σ_R). Two more excavation cycles will put some elements on the tension cutoff yield surface but a fracture will not initiate (Figure 4.9b). The explanation is that while yielding has occurred, the "stress intensity factor" has not reached its critical value. During the next excavation cycle (Figure 4.9c), a fracture initiates and propagates to 60% of the core radius (9 elements).

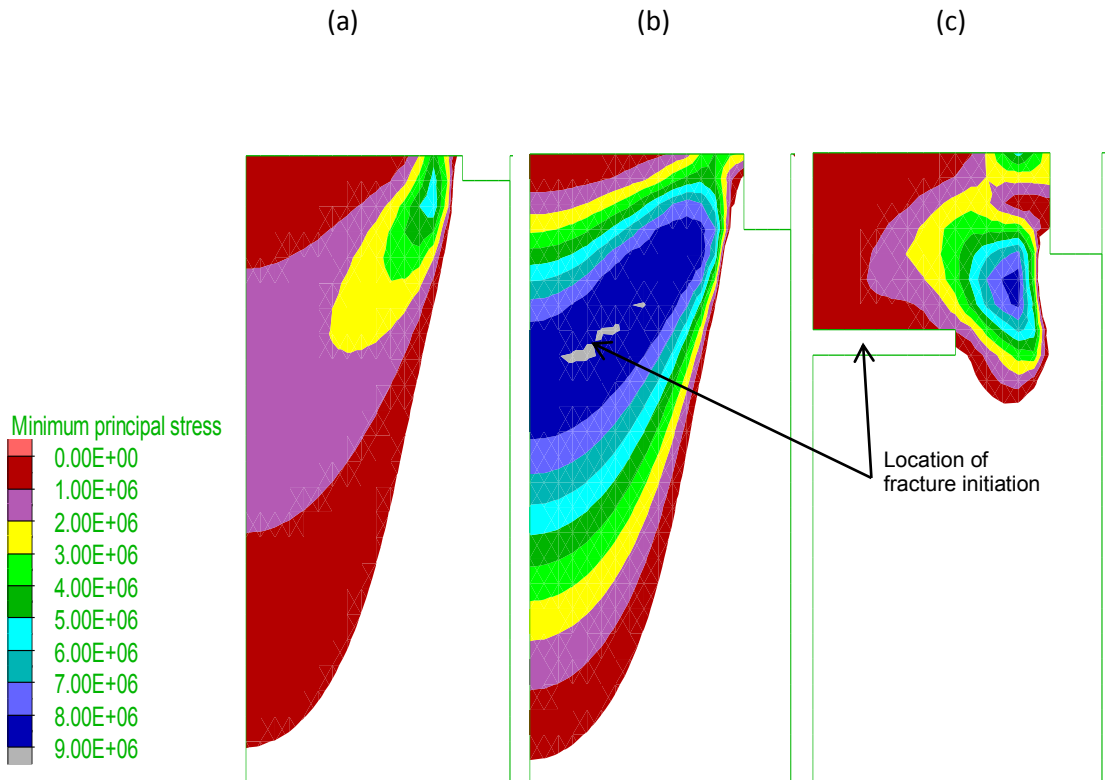

Figure 4.9: Evolution of minor principal stress distributions (tensile only) during excavation. The excavation depths are (a) z = 0.067 R, (b) z = 0.2 R, and (c) 0.267 R.

To determine the radial location of fracture initiation, the tensile strength values of all 9 elements were tracked during the excavation. While all nine elements softened almost instantaneously, the two elements at radial distances 0.23 R (4 elements) and 0.3 R (5 elements) softened first. This implies that the fracture initiation occurred around 0.267 R, placing the disking situation into Stage 1 as defined in the Elastic Analysis section (3.2.1).

Initially, the fracture displays unstable behavior (Equation 4.6) since the fracture propagates to 60% of the core radius without any change in the "stress intensity factor". It should be noted that since the coring process keeps the nominal stress constant, change in geometry is required to increase the "stress intensity factor". In more traditional experiments, three-point bending for example, the opposite occurs where an

increase in nominal stress increases the "stress intensity factor" and the geometry remains constant.

$$\frac{dK}{da} < 0 \tag{4.6}$$

Next, the stress profile of the fracture is analyzed and displayed in Figure 4.10. The characteristic length (Equation 3.19) is defined as the length of the fracture process zone, 1.96 R (47.1 mm). Physically, this identifies the length of the damaged zone and this should be represented in the model.

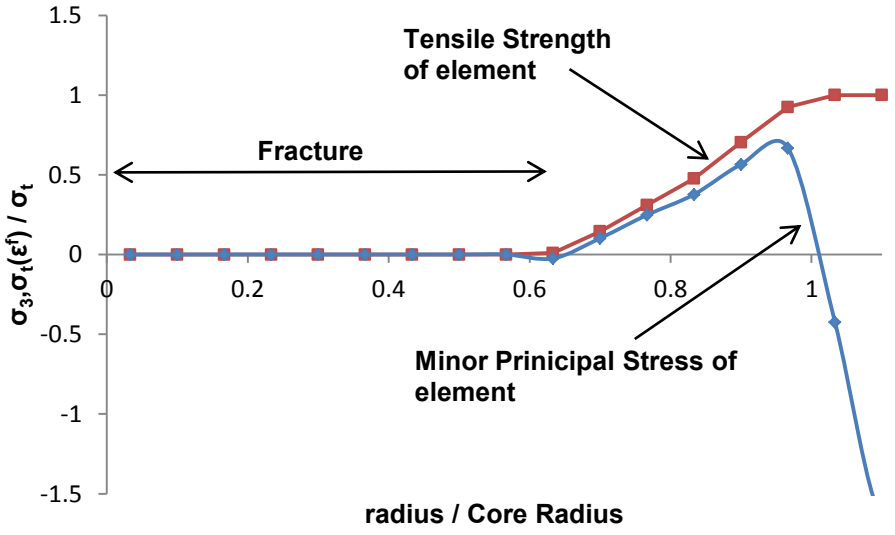

Figure 4.10: Stress profile of crack.

Due to a complex stress state, the minor principal stress becomes compressive around 0.4 R from the crack tip. This also is the length of the damaged zone, which is smaller than the characteristic length. From this information, it is difficult to conclude how the characteristic length will affect the disking process. Yet, as can be seen, the minor principal stress tends to closely follow the tensile strength. This implies that any new tensile stress increase from a change in geometry should further propagate the crack.

Once a mode I fracture appears, one method of predicting the future fracture path is by observing the direction of the major principal stress. From the stress state of the element

next to the crack tip, the major principal stress has an orientation of 3°, counterclockwise positive from the x-axis. This implies that the fracture will propagate out radially but also slightly upwards. In the literature, disking is usually not completely horizontal but has a slight concave nature [5,22]. These observations are verified by the model but due to the grid layout, no visual curvature will be observed.

Excavating further, the fracture will act in a stable manner and propagate towards the excavation path, eventually creating a completely separated disk, essentially "resetting" the problem. Further excavation will then repeat the entire process, creating disks of around the same thickness.

However, at least two factors have a determining role in fracture initiation depth and this can cause inconsistent disk thicknesses in a deterministic homogenous model. First, with each disk creation, the initial geometry changes causing slightly larger stress magnitudes during the initial excavation process (Figure 4.11). This explains the initially decreasing thicknesses in Figures 4.4 and 4.6 in the Mohr-Coulomb section (4.1) and why the elastic disking criterion differs from previous elastic analyses (Figure 4.12) [16]. After a particular depth, the stress magnitudes should remain constant. Second, yielding prior to fracture may have an effect on the disk thickness. In previous analyses it was shown that yielding below the fracture during the initial excavation cycles can play a role in determining the disk thickness [16]. These effects were not significant in this particular analysis but this may still potentially play a role.

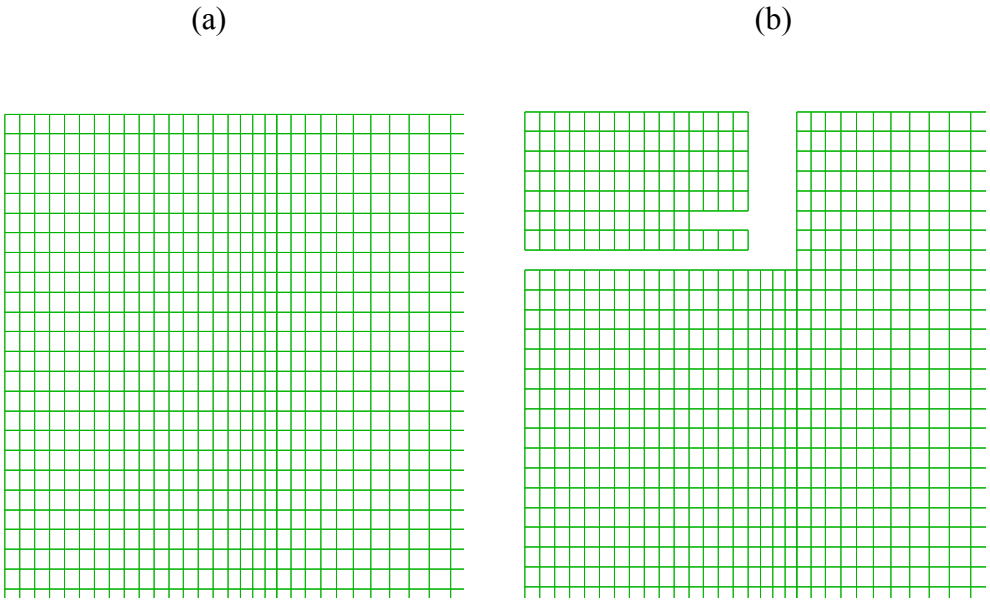

Figure 4.11: Comparison of initial geometries after first disk creation

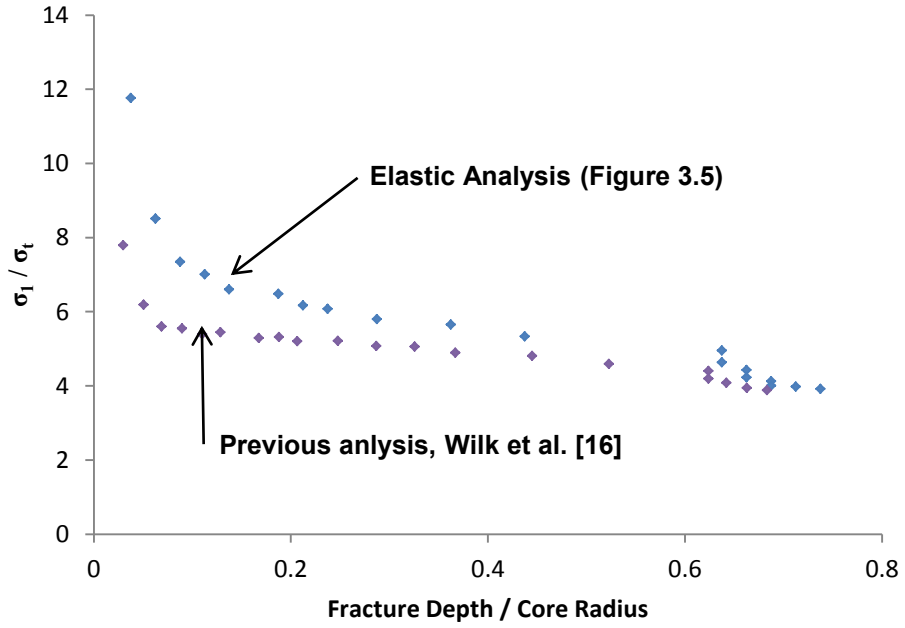

Figure 4.12: Comparison of stage one and two of the elastic analysis with strength limits disking criterion (Figure 3.4) for different initial geometries. In Wilk et. al (2012), the external boundary is high enough where further disking will not affect elastic magnitudes and distributions [16].

While the described behavior was observed for a particular situation, different geometries and *in-situ* stresses can produce different results. As described in the elastic analysis, the location of maximum tensile stress begins near the core boundary and free surface. As the excavation proceeds, it moves diagonally through the core increasing in depth and decreasing in radial distance. If the applied radial stress is increased, the critical stress intensity factor is reached earlier in the excavation process. This will cause fracture initiation to occur at a greater radial distance and depth, decreasing disk thickness. If the applied radial stress is decreased, the fracture initiation will occur along the core center and at a greater depth, increasing disk thickness. The maximum simulated disk thickness is around 0.6 R.

While the elastic analysis predicts large tensile stresses along the boundary in stage three, no fractures were observed to initiate from the core boundary. The explanation is that while a high tensile stress magnitude exists, the area of that stress region is so small that the stress intensity factor could not reach a critical value. In other terms, the strain energy was not enough to produce a fracture. This implies that while an elastic analysis with strength limits can be useful, such as in predicting fracture orientations [3,45], care must be taken if the maximum tensile stress is concentrated in a small region since it may not be the location of fracture initiation.

4.4 Disking Relation

The main impetus behind core disking research is to indirectly measure the *in-situ* stress state, so determining a general relation between disk thickness and stress magnitude is desirable. Since simulated Georgia granite results were matched against the experimental results from Obert and Stephenson, an attempt will be made to determine a disking relation for Georgia granite. This relation cannot be verified since Obert and Stephenson only determined the disking initiation stress. However, field results of Lac du Bonnet granite and granodiorite at the URL Tunnel in Canada, which displayed similar strength properties, can be used as a reference [22].

From the field study, it appears disk initiation stress magnitudes, around seven times the tensile strength, produce a variety of disk thicknesses, ranging from 0.8 to 4.4 times the core radius. Increasing the maximum principal stress will decrease the disk thickness until the grain size is reached, which occurred at around 11 times the tensile stress. At stress ratio levels greater than 11, the disk will appear crushed into multiple pieces [22]. From these observations, Lim and Marin adopted the following empirical relation for Lac du Bonnet granite and granodiorite,

$$\sigma_1 = A + \frac{B}{\exp(\frac{t}{C})} \tag{4.6}$$

where σ_1 = the major principal stress, t = disk thickness, and A, B, and C are curve-fitting parameters. Advantages of this relation are that it allows for a disking initiation stress (A), a stress ceiling ($A + B$), and a variety of curves to fit the particular exponential relation (C).

To determine the relation for Georgia granite, simulations were performed at intervals of 0.55 σ_t (5 MPa) ranging from 6.6 – 11.5 σ_t (60 – 105 MPa) for a core radius of 24 mm. This range was chosen since disking did not occur below 6.6 σ_t (60 MPa) and stresses above 11.5 σ_t (105 MPa) would cause the entire structure to fail. Figure 4.13 shows the numerical data compared against best fit relations from Lac du Bonnet granite and granodiorite [22].

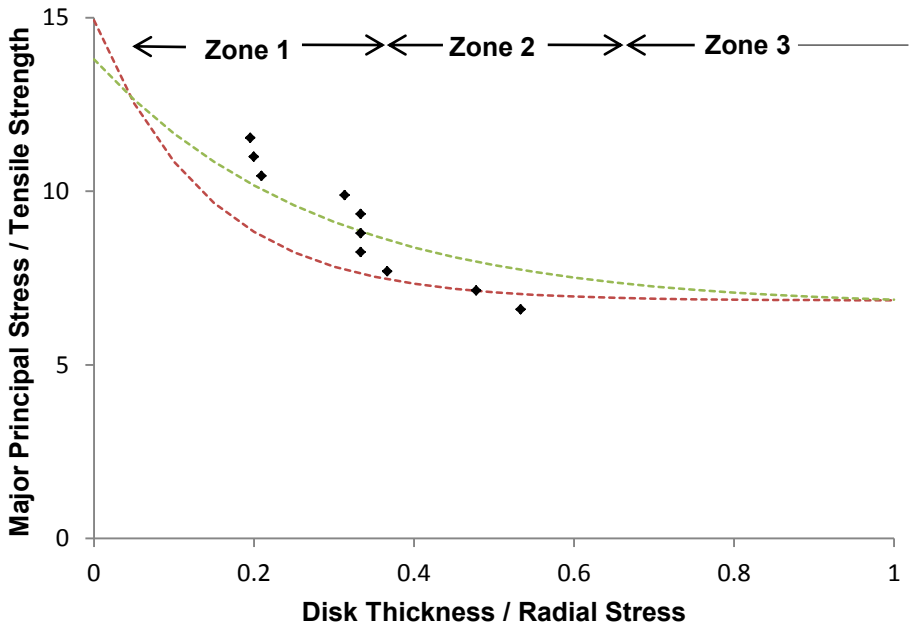

Figure 4.13: Simulation data showing relation between normalized radial stress and disk thickness.

Lim and Martin suggested three stress zones for the relation [22]. The first zone (< 0.4 t/R), a high stress region, displays large changes in stress for small changes in disk thickness. The second zone (0.4 – 0.8 t/R), medium stress region, displays moderate changes in stress. The third zone (> 0.8 t/R), the core disking initiation stress region, showed little to no changes in stress for a wide range of disk thicknesses.

The numerical simulation seems to be able to replicate the first two zones to a reasonable degree, but not the third. This is most likely due to the third zone being dependent on heterogeneity or statistical effects, an aspect not taken into account in a deterministic homogenous model. This will be explored later in the thesis.

One issue that arises is determining which parameter should be best fit with the data and which should be set to a particular value. Parameter *A* represents the disking initiation stress so it should be set as such. Parameter *B* represents the difference between the stress magnitude that would theoretically produce a disking thickness of zero (stress ceiling) and the disking initiation stress. Physically, a disk thickness of zero can never be achieved since disking will not be thinner than the grain size. Whether the value of

Parameter *B* should be set or best fit is up for interpretation since the stress ceiling usually cannot be determined from simulations. Field results suggest a stress ceiling of 13 σ_t or 14 σ_t but large variations may be observed for different rock type. Parameter *C* determines the curvature of the function so this should be best fit with the simulation results.

Multiple best-fit parameters were tried, each with a different *B* value. The first relation (Relation 1) will solve for *B* as best-fit parameter. The second relation (Relation 2) will set for a value of *B* assuming a linear relation of data points in Zone 1. The third relation (Relation 3) will set *B* so that the stress ceiling for Georgia granite and Lac du Bonnet granodiorite are equal at 13.9 σ_t. The best-fit parameters and corresponding R^2 values are displayed in Table 4.5 and the relations are shown in Figure 4.14. Figure 4.14 compares the three best-fit relations with the best-fit relations of Lac du Bonnet granite and granodiorite.

Table 4.5: Parameters and corresponding R^2 values for all three relations.

Relation	A	B	C	R^2
1	6.59	14.7	0.168	88.8%
2	6.59	10	0.224	84.1%
3	6.59	7.20	0.294	73.6%

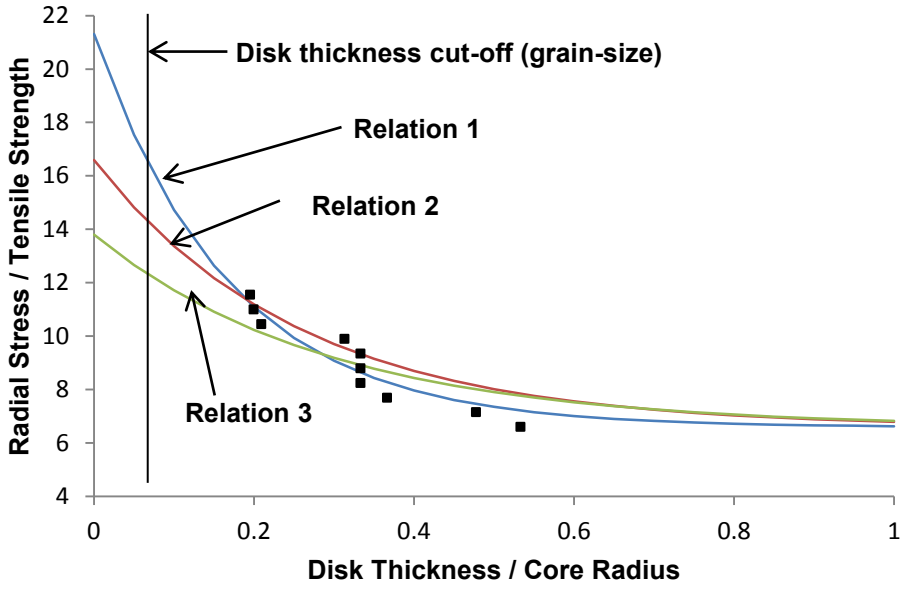

Figure 4.14: Three different best-fit relations for the simulation data.

Depending on the relation, extrapolating to predict the stress magnitude that produces disk thickness of a grain size results in variation of stress magnitudes from 12.5 σ_t to 16.5 σ_t. This reinforces the claim that large error will exist if attempts are made to predict stress magnitudes from extremely thin disks [22]. More field and laboratory studies will be extremely useful to help verify a disking relation.

4.5 Size Effect

Core disking literature often normalizes disk thickness by the core radius or diameter [22]. While being the most obvious length scale, its normalization implies a lack of size effect, defined as when the nominal stress required for failure changes for two differently sized, but geometrically similar structures. A size effect can be attributed to microcracks within the core. Assuming a homogeneous structure, thus eliminating statistical size effect, two types of energetic size effects exist: Type I size effect, from crack initiation, or Type II size effect, from an existing notch or fracture [31].

Type one size effect, which is expected for core disking, occurs from crack initiation. Before a fracture initiates, microcracks form in the fracture process zone (FPZ), which is responsible for the scaling effect. For core disking, due to the complicated geometry and failure mechanism, the stress intensity factor function is currently undefined.

For this reason, scaling relations must be solved either experimentally or numerically and cannot be checked by an analytical solution until a stress intensity factor is established. To numerically solve for a scaling relation, geometrically similar structures are required. In core disking, geometrically similar structures would assume a constant ratio between disk thickness, core radius, and length and depth of excavation path (t:R:w:z). In most size effect experiments, the crack location is known either by placement of a notch (Type II) or from a region of maximum stress (Type I). Therefore, observations can be made by standard force or displacement controlled tests on specimens of proportional size. In core disking, however, the region of maximum tensile stress will move as the excavation proceeds so the crack location is unknown with respect to both the radial distance and depth. Also, the influence from stress path prevents experiments from simply excavating to a certain depth then increasing radial stress until a fracture occurs. Even so, this would still not guarantee geometrically similar structures since the relation between disk thickness and excavation depth is non-linear.

This forces size effect analyses to be approached in an inverse fashion, measuring a change in geometry (t/R) for a particular nominal stress. Inverting the results then gives standard size effect notation. As mentioned earlier, t:R:w:z can never truly be constant for different radii since t:z is non-linear, therefore the structures can never actually be geometrically similar. The effects, however, should be negligible so the excavation depth factor was discarded. Radial length of excavation path (w) was proportioned with core radius during numerical simulations (t/w will always be constant) so geometrically similar structures in core disking just assume a constant t/R.

Figure 4.15 illustrates two geometrically similar structures in core disking, where the core radius and disk thickness are equal. Another normalizing parameter is characteristic length. Since characteristic length is assumed to be a material property, a size effect relation can be determined for a constant disk thickness from various core radii. Figure 4.16 references this second geometry.

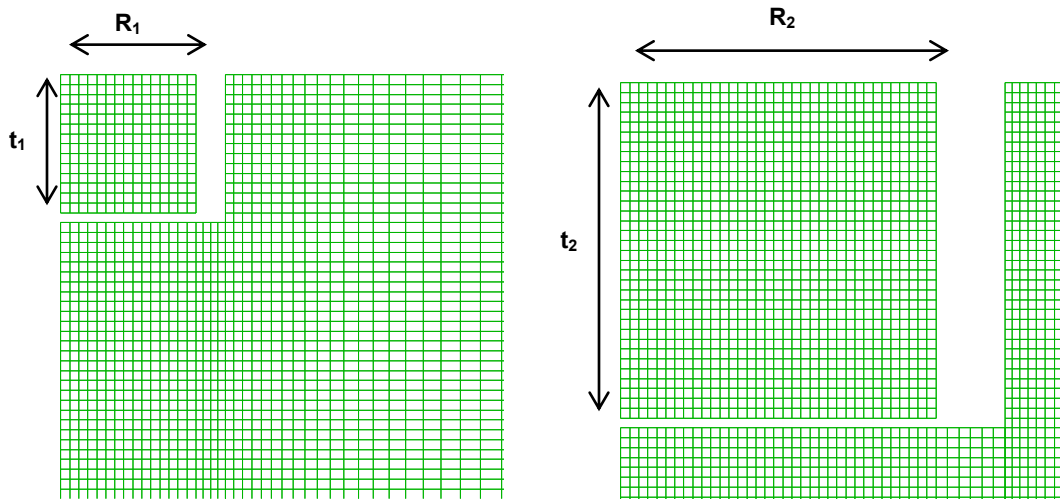

Figure 4.15: Two geometrically similar structures with t/R = 1.0

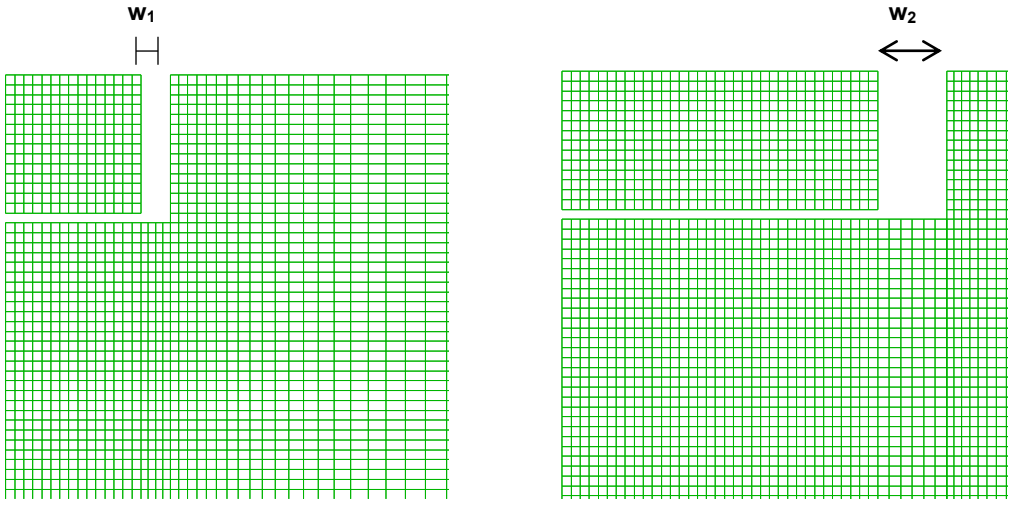

Figure 4.16: Two structures with proportional t/ℓ_{ch}.

To determine size effects, various radial stresses were simulated in intervals of 0.55 σ_t (5 MPa) from the disk initiation stress until a maximum is reached through block failure

or limitations from element size, on different core radii: 0.51 ℓ_{ch} (24 mm), 0.68 ℓ_{ch} (32 mm), 0.85 ℓ_{ch} (40 mm), 1.19 ℓ_{ch} (56 mm), and 1.53 ℓ_{ch} (72 mm). As in the previous section, a best-fit relation was determined for each core radius and this is plotted in Figure 4.17. The first plot shows the relation between radial stress, normalized by tensile strength, and disk thickness, normalized by core radius, while disk thickness is normalized by characteristic length in the second plot.

(a)

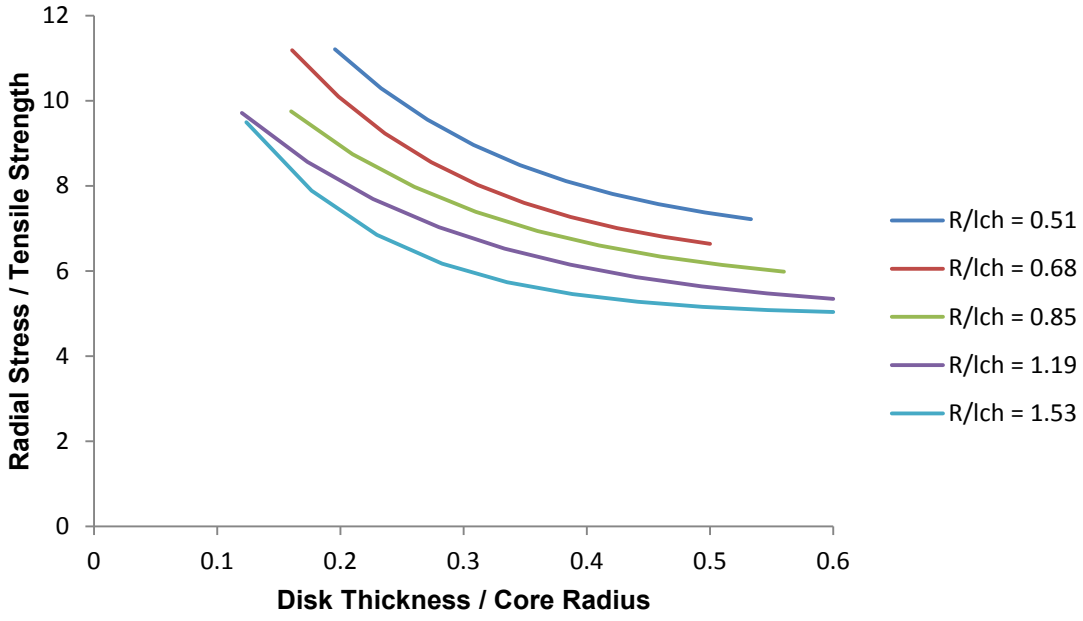

(b)

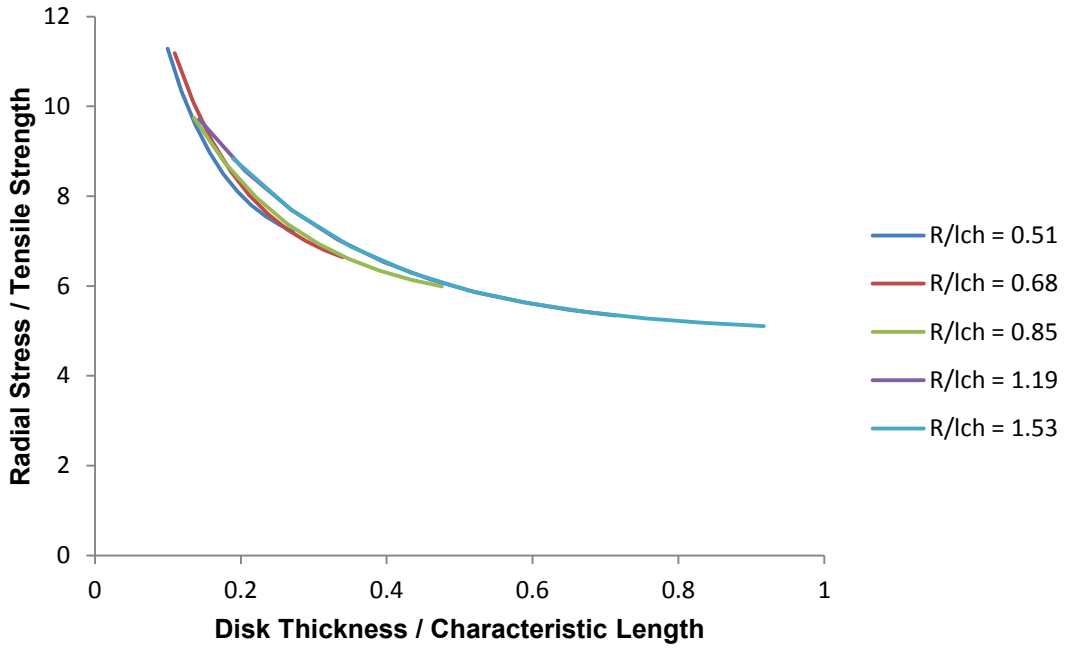

Figure 4.17: Comparison of size effect for various core radii for (a) geometrically similar and (b) constant disk thickness situations

From Figure 4.17a, the nominal stress for geometrically similar structures does change for differing core radii, implying a size effect. However, the nominal stress for constant disk thickness does not change for differing core radii, suggesting that core radius has an indirect or no influence on the stress level required for disking. However, larger core radii produce proportionally larger disk thicknesses. Normalizing by core radius limits disk thickness to 0.6 R for all core radii.

From the results, a simple normalization parameter does not exist. While normalizing by core radius shows a size effect, disking relations for different rock are similar. For example, the 2 mm or so average grain size of Lac due Bonnet granite and 0.75 mm average grain size of Lac du Bonnet granodiorite produced similar parameter *C* values (0.14 to 0.28) in the disk relation. When normalizing by characteristic length, the parameter *C* values become very different, 1.6 to 8.4.

4.6 Calcarenite: Preliminary Results

One of the end goals of research on core disking is to create a criterion or numerical model that not just replicates the disking process, but predicts the disk thicknesses and fracture orientation. While disking did not occur for the Calcarenite specimens, the preliminary numerical results are still presented to discuss potential difficulties in disk thickness prediction.

Since an appropriate constitutive model has been established for flat core disking, material characterization remains the largest uncertainty for prediction. To date, most numerical models have either simulated core disking using a heuristic approach [13] or looked into the process using hypothetical rock properties [12]. While this shows that it is ideally possible to predict disk thicknesses, complete material characterization is not available from any experiment or field study. Therefore, it is not certain that plugging in tested material parameters will guarantee accurate results.

A large reason to currently doubt the predictive ability of these models is the dependence on tensile strength and fracture energy. Experiments determining both of these properties are more difficult to run that most compression tests and interpretation of results can lead to a wide range of values. For Calcarenite, tensile strength was determined using the direct tensile strength and fracture energy was calculated using the assumption of linear elastic fracture mechanics from the critical stress intensity factor. Figures 4.18 and 4.19 display the numerical prediction results.

(a) (b) (c)

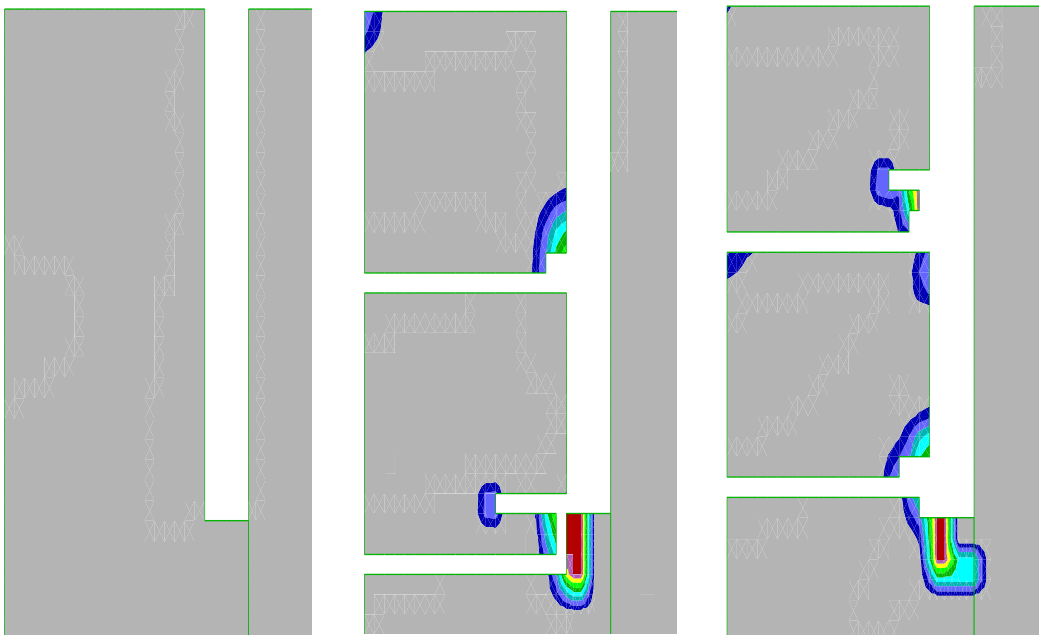

Figure 4.18: Contours of tensile strength for (a) 4 σ_t (10 MPa) (b) 4.4 σ_t (11 MPa), and (c) 5.2 σ_t (13 MPa).

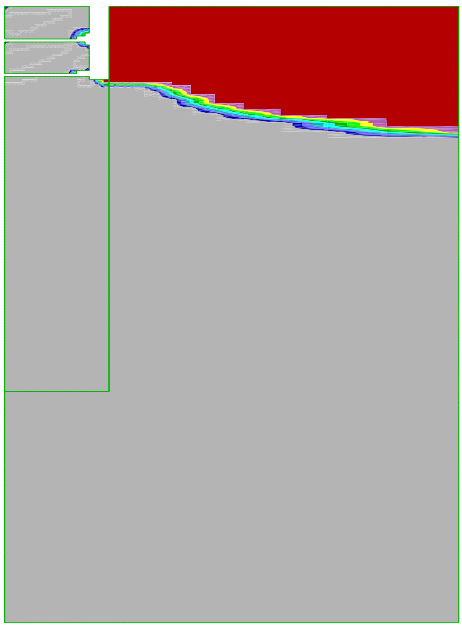

Figure 4.19: Contour of tensile strength for 5.6 σ_t (14 MPa).

As can be observed in Figure 4.18, disking was predicted to occur from a range of 4.4 – 5.2 σ_t (11 – 13 MPa), well below the expected disking initiation stress of around 7 σ_t (17.5 MPa). An explanation for this low predicted disking initiation stress is the low fracture energy value, which was shown earlier to lower the required radial stress for disking. The low fracture energy value likely occurred due to the assumption that linear elastic fracture mechanics can apply, which in turn assumes a brittle material. Assuming a quasi-brittle material, the fracture energy value would be higher, giving a larger disking initiation stress.

Another reason to doubt the results of such a low fracture energy value is the lack of damage predicted to occur for an applied radial stress of 4 σ_t (10 MPa). If 0.4 σ_t (1 MPa) separates disking from no damage, it implies an extremely brittle material. Since damage was experimentally shown to occur within the core, it can be concluded that linear elastic fracture mechanics may not be an appropriate assumption when predicting the fracture energy for core disking.

A final issue with performing core disking experiments on low strength materials is the possibility of failure of the block, as seen in Figure 4.19. If the block fails, a displacement will occur along the block boundary causing the pressure in the flat-jacks to become unevenly distributed possibly ruining the apparatus. To avoid this event from occurring, conservative stresses were applied to the Calcarenite specimens.

4.7 Core Damage

While disking shows that damage can occur to the core during the excavation process, there is little known about the stress levels that initially cause damage and whether they affect laboratory tests of material parameters. For this analysis, it was assumed that damage occurs when the tensile yield surface is reached. Therefore, while the disking criterion in the elastic analysis with strength limits section should suffice, it simulates the elastic response when excavating from a free surface. In practice, the core should

have already reached its steady-state stress distribution when entering stress levels large enough to cause damage. Referencing Figure 3.4, when disk thicknesses are over 2.0 R, the normalized maximum tensile stress is around 0.2 in the core center and 0.4 along the core boundary. For the Georgia granite, that implies that damage should occur along the core boundary at 2.5 σ_t (22.8 MPa) and in the core center at 5.0 σ_t (45.5 MPa).

To view how core damage is simulated in the numerical model, radial stresses of 6.0 σ_t (55 MPa) and 3.8 σ_t (35 MPa) are applied to the boundaries. Figures 4.20 displays the tensile strength (functions of plastic strain) contours while Figure 4.21 displays the minor principal stress contours (tension only).

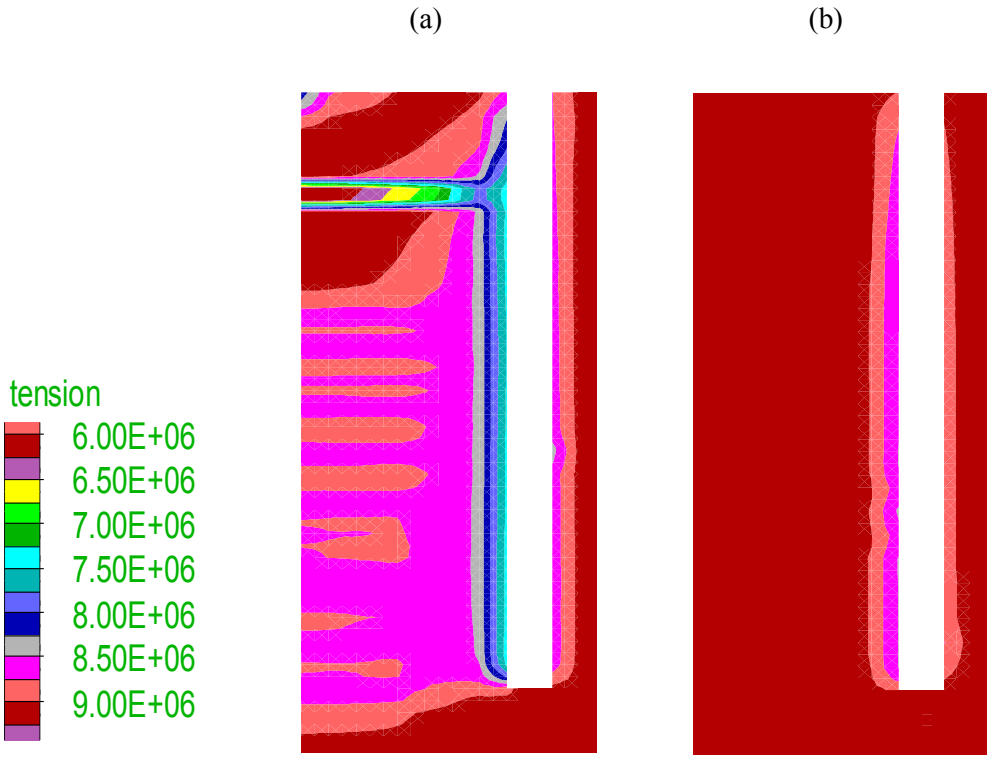

Figure 4.20: Tension contours for (a) 6.0 σ_t (55 MPa) and (b) 3.8 σ_t (35 MPa).

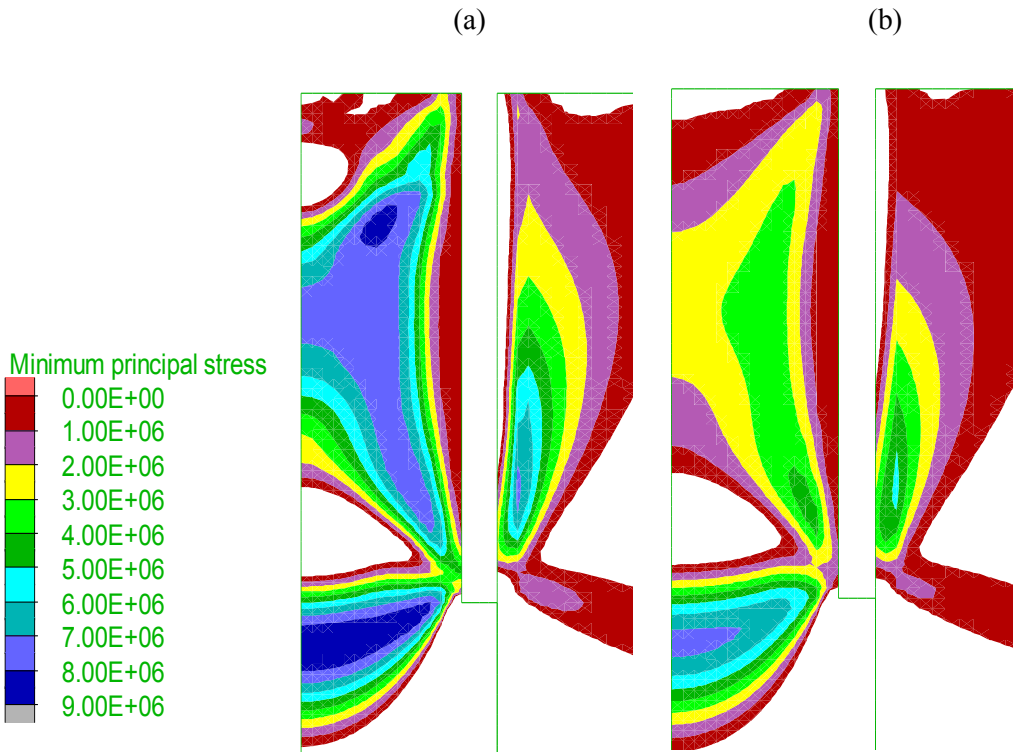

Figure 4.21: Minor prinicpal stress contours (tension only) for (a) 6.0 σ_t (55 MPa) and (b) 3.8 σ_t (35 MPa).

The tension contours match the predicted results. For 6.0 σ_t (55 MPa), a band of damage appears near the top of the core and then the rest of the core appears to be more or less uniformly damaged. It has been observed in field studies [22] and experiments [5], that white rings often appear in the cores that have been excavated slightly below the disking initiation stress. While the rings repeat itself in regular intervals, unlike in the numerical model, the mechanism may be similar. The most damaged element in the band retains 33% of its tensile strength of 3.012 MPa.

Since core damage will likely occur during a steady state condition, the rest of the core retains around 90% of its tensile strength of 8.3 MPa. Unlike the elastic analysis, the stress region in the core center is much flatter and expands throughout the core center. This implies that the amount of damage should be equal throughout the core. The core boundary experienced slightly higher levels of damage, retaining 80% of its tensile strength of 7.4 MPa. It can be seen that the tensile stress region along the boundary

almost disappears in the elasto-plastic analysis. It is also interesting to note that fractures do not occur from an excavation that reaches stage three despite the high tensile stress observed in the elastic analysis. Due to the small area and high stress gradient associated with that stress region, a conceptualized stress intensity factor may never reach the critical value, not initiating or propagating a fracture.

For 3.8 σ_t (35 MPa), as predicted, the stresses in the core center are not large enough to yield the rock but yielding still occurs along the core boundary, with elements retaining 92.5% of the tensile strength of 8.45 MPa. This low level of damage occurs only within a small area so it would not be expected to affect material properties using mechanical or ultrasonic methods. It should also be noted that damage does not occur for low levels of stress 1.6 σ_t (35 MPa).

A question that arises from these results is the consequence of a damaged core. While it is shown that damage can affect the material properties, the threshold where damage becomes significant is unknown. Unfortunately, continuum numerical simulation cannot address this question. Once a yield surface is reached, plastic strain accumulates in elements, which can give insight into when damage can occur, but it cannot translate into degradation of material properties unless specified by the user prior to the analysis.

Another issue possibly occurs from simplified constitutive relations. Since the modified Mohr-Coulomb failure criterion models macro-structural behavior, where the yield surface is set as the peak stress level, it is inherently insufficient for modeling microstructural effects. It is well understood that crack initiation occurs well before peak stress in compression [23,40], and assuming the same effect occurs in tension, accurately assessing damage requires a constitutive model that incorporates crack initiation as well as peak stress.

Chapter 5: Conclusions and Recommendations

5.1 Summary

To determine material properties of rock, it is currently required that engineers excavate to the location of interest in order to extract material for laboratory evaluation. During this process, it is usually assumed that the extracted rock is not damaged by the excavation (coring) process, therefore being a representative sample of the *in-situ* rock. However, since extraction implies that the core must be unloaded from a stressed state, it is possible the core experiences a damage inducing stress path, potentially fracturing through the entire core cross-section. This led to the speculation that these drilling-induced core fractures can potentially estimate in-*situ* stress and that material property degrading core damage can still occur in situations where these fractures did not appear. To investigate this phenomenon, laboratory experiments and numerical simulations were performed, replicating the coring process in a stressed medium.

To predict the *in-situ* stress state, a relation is developed between the disk thickness, interval length between fractures, and magnitudes of a simplified stress state: the horizontal stresses are equal to the radial stress $\sigma_r = \sigma_H = \sigma_h$, and the vertical stress is zero $\sigma_v = 0$. As the radial stress σ_r increases, the disk thickness has been observed to decrease. Also, in order for these disking fractures to occur, a certain stress threshold, called the disking initiation stress, must be surpassed.

Experimentally, one core was excavated from a block of Boise sandstone and three cores were excavated from three blocks of Calcarenite, each experiencing a different magnitude of radial stress. Disking was observed in the Boise sandstone but not in the Calcarenite. For the Calcarenite samples, various indicators showed signs of damage and the Young's modulus was lower when compared with core samples excavated in a block that was not stressed during coring.

Numerically, core disking experiments on Georgia granite performed by others were simulated. The objectives were to determine (1) a constitutive relation that can replicate the disking process for large ranges of radial stress magnitudes, (2) relate disk thickness with radial stresses and verify results with field results, (3) identify important aspects of the failure process, and (4) investigate the use of numerical methods as predictive tools for *in-situ* stress magnitudes.

The use of various constitutive models shows that the tension softening (TS) model was able to reproduce the effects of core disking for a wide range of radial stresses. Since disking results from a tensile failure mechanism, the TS model promotes yielding in tension by eliminating the shear failure mode of the modified Mohr-Coulomb failure criterion. This allows disking to occur over a wide range of radial stresses, decreasing in thickness as radial stress is increased, and without influence from a shear failure mode.

While initially experiencing compressive principal stresses, the unloading process produces tensile stress regions in the core that change in location and magnitude as the excavation proceeds. Yielding will occur when the tensile stresses in the core reach the yield surface. Tensile failure is associated with Mode I fracture, so initiation and propagation should be related to a stress intensity factor. Due to the complexity of the stress paths and the unknown crack length, an analytical expression for the stress intensity factor was not attempted, but instead a smeared cracking approach was used to model fracture by simulating the degradation of tensile strength as plastic tensile strain accumulates within an element.

The location of fracture initiation was identified for a variety of radial stress magnitudes and core radii. Following the elastic analysis, large radial stress magnitudes ($>10\ \sigma_t$), where σ_t is uniaxial tensile strength, will initiate fractures at low depths and larger radial distances, but not at the core boundary. These fractures are generally unstable until reaching the core boundary and usually propagate radially with almost no curvature. As the radial stress is decreased, the location of fracture initiation follows the stress path observed in the elastic analysis, with depth increasing and radial distance decreasing.

The fractures display stable behavior, initially propagating to lower percentages of the core radius, and slightly upward curvature is expected. As the disking initiation stress is reached, a maximum depth of fracture initiation occurs along the core center at 0.6R, where R is the core radius. The elastic analysis predicts a second tensile stress region developing along the core boundary, but no fractures were observed to initiate from that location.

Radial stress and core radius were checked as possible factors that can influence the disking process. For the axisymmetric biaxial stress state ($\sigma_H = \sigma_h$, $\sigma_v = 0$), increases in radial stress result in a decrease in disk thickness. When simulating Georgia granite, the numerical relation matches the trend from field data of Lac du Bonnet granite and granodiorite, which are similar in material properties with the Georgia granite. However, the deterministic, homogenous model was not able to predict the large disk thicknesses (0.8 – 4.0 R) that occur around the disking initiation stress. These large disk thicknesses are most likely attributed to heterogeneity or weak planes in the rock. Also, it seems that core radius does not have a significant influence on disk thickness.

Previous research found fluid pressure to have an effect on disking and while not investigated, characteristic length, anisotropy, thermal effects, and drilling mud will most likely play a role. One advantage of numerical models is that each core disking situation can be modeled independently.

5.2 Future Work

The ultimate objective of core disking research is to create a method of predicting *in-situ* stress states from drilling-induced fracture patterns. This thesis provides the basic groundwork of an elasto-plastic analysis for the simplest drilling induced fracture, flat core disking, under an axisymmetric biaxial stress state ($\sigma_H = \sigma_h$, $\sigma_v = 0$).

Other researchers have performed an elastic three-dimensional analysis that predicted the tensile fractures trajectories in boreholes, and found that if alternative stress states are considered, drilling-induced fracture may take various forms: saddle-shaped

disking, petal fractures, and petal-centerline fractures. For example, flat disking is predicted in thrust fault stress regimes ($\sigma_H \geq \sigma_h \geq \sigma_v$) when σ_H and σ_h are relatively equal. As σ_H increases, creating unequal horizontal stresses, saddle-shaped disking occurs. Other fault regimes, normal ($\sigma_v \geq \sigma_H \geq \sigma_h$) and strike-slip ($\sigma_H \geq \sigma_v \geq \sigma_h$), tend to produce petal and petal-centerline fractures.

Currently, these various types of drilling-induced fractures can give insight into the general fault regimes and can potentially be expanded to a three-dimensional elasto-plastic analysis. However, while the mesh layout for the axisymmetric biaxial case was not an issue since the fracture follows the mesh layout, these other types of drilling-induced fractures will not, complicating the analysis.

The largest remaining uncertainty to numerically predict *in-situ* stress magnitudes from disk thickness is the effect from material properties. Tensile strength and fracture energy are two important parameters in disking, but their values are difficult to obtain and various interpretations and assumptions can lead to wide range of values.

In summary, a pressing issue in drilling deeper underground is the measurement of *in-situ* stress states. Since a "silver bullet" solution to stress state measurement is unlikely, engineers will need to diversify their techniques and incorporate multiple direct and indirect measurements to piece together the stress state. While only in the early stages, core disking serves as a potential indirect method that can be used alongside others, such as borehole breakouts, to assist in *in-situ* stress state prediction.

Another potential use of core disking analysis is the determination of localized areas of high in-situ stress. It has been recognized that the assumption of homogeneous *in-situ* stress throughout an underground structure may not be acceptable, and the occurrence of core disking or a sudden decrease in disk thicknesses can give insight into local areas of high lateral stresses.

A final implication from core damage is not only the prediction of *in-situ* stress, but the strength parameters assigned to the intact rock. Intact rock strength is fundamental for

underground structural design. The inability to obtain a sample of the rock mass without damaging the rock remains an important obstacle to overcome. Knowledge, or at least recognition, of the effects of excavation induced damage can potentially lead to a better understanding of the rock mass itself and the ability of engineers to predict responses.

References

1. Fairhurst, C. Stress estimation in rock: a brief history and review. *Int J Mech Min Sci.* 40(2003): 957-973
2. Christiansson, R. The Latest developments for *in-situ* rock stress measuring techniques. *Proceedings of the International Symposium on In-situ Rock Stress*, Trondheim, Norway (2006), pp. 3–10
3. Li, Y.Y., D.R. Schmitt. Drilling induced core fractures and in situ stress. *J Geophys Res* 1998;103(B3):5225–39
4. Jaeger, J.C., N.G.W. Cook. Pinching-off and disking of rocks. J Geophys Res 1963;68(6):1759–65
5. Obert, L., D.E. Stephenson. Stress conditions under which core disking occurs. *SME Trans*., 232, 227-235, 1965.
6. Stacey, T.R., Contribution to the mechanism of core discing, *J. S. Afr. Inst. Min. Metall*., 82, 269-275, 1982
7. Dyke, C.G. Core disking: Its potential as an indicator of principal in situ stress directions, in *Rock at Great Depth*, vol. 2, edited by V. Maury, and D. Fourmaintraux, pp. 1057-1064, A.A. Balkema, Brookfield, Vt, 1989.
8. Li, Y.Y., D.R. Schmitt. Effects of poisson's ratio and core stub length on bottomhole stress concentrations. *Int J Mech Min Sci*. 34 (1997): 761-773
9. Kaga, N. K. Matsuki, K. Sakaguchi. The in situ stress states associated with core discing estimated by analysis of principal tensile stress. *Int J Mech Min Sci.* 40 (2003): 653-665
10. Matsuki, K., N. Kaga, T. Yokoyama, N. Tsuda. Determination of three dimensional in situ stress from core disking based on analysis of principal tensile stress. *Int J Mech Min Sci*. 41(2004): 1167-1190
11. Lim, S.S., C.D. Martin, R. Christiansson. Estimating *in-situ* stress magnitudes from core disking. *Proceedings of the International Symposium on In-situ Rock Stress*, Trondheim, Norway (2006), pp. 159–166
12. Hakala, M. Numerical study of the core disk fracturing and interpretation of the in situ state of stress. In: Vouille G, Berest P, editors. Ninth congress of international society for rock mechanics. Paris, vol. 2. Rotterdam: A.A. Balkema; 1999. 1149-53.

13. Corthésy R. M.H. Leite. A strain-softening numerical model of core discing and damage. *Int J Mech Min Sci*. 45(2008): 329-350.
14. Valley, B. N. Bahrani, P.K. Kaiser. Rock strength obtained from core samples and borehole wall instabilies – the effect of drilling induced damage. In: Proceedings of European Rock Mechanics Symposium EUROROCK. Lausanne, Balkema. 2010.
15. Jiang, A.N., and Z.W. Zeng. Three dimensional numerical simulation of rock core discing based on strain soft model. *Adv Mat Res.* 187(2011): 565-569
16. Wilk, S.T., C. Fairhurst, J.F. Labuz. Issues with numerical simulation of core disking. *46th U.S. Rock Mechanics Symposium*. 24 – 27 June. 2012. Chicago, IL.
17. Zhu, W., G. Li, K. Wang. Analyses of disking phenomenon and stress field in the region of an underground powerhouse. *Rock Mech Rock Eng.* 18(1985): 1-15
18. Ishida, T., T. Saito. Observation of core discing and in situ stress measurements; stress criteria causing core discing. *Rock Mech Rock Eng.* 28(1995): 167-182
19. Song, I., B.C. Haimson. Core disking in Westerly granite and its potential use for in situ stress estimation. In: Amadei B, Kranz RL, Scott GA, Smeallie PH, editors. Proceedings of 37th U.S. Rock Mechanics Symposium, Colorado, 1999. vol. 2. Rotterdam: A.A. Balkema; 1173-80.
20. Takehiro, S. Core disking and "rock burst" in soft tuffaceous rock masses at iwate tunnel. *QR of RTRI,* Vol. 42, No.3, Sept. 2001. 130 – 135.
21. Bunger, A.P. Stochastic analysis of core disking for estimation of in situ stress. *Rock Mech Rock Eng*. 43(2010): 275 – 286
22. Lim, S.S., C.D. Martin. Core disking and its relationship with stress magnitude for Lac du Bonnet granite. *Int J Mech Min Sci*. 47(2010): 254 – 264
23. Eberhardt, E., D. Stead, B. Stimpson. Effects of sample disturbance on the stress-induced microfracturing characteristics of brittle rock. *Can Geotech J*. 36(1999): 239-250
24. Lanaro, F., T. Sato, S. Nakama. Depth variability of compressive strength test results of Toki granite from Shobasama and Mizunami construction sites, Japan. *Rock Mech Rock Eng*. 42(2009): 611-629
25. Kenter, C.J., M. Brignoli, R.M. Holt. CMS (Constant Mean Stress) vs UCS (unconfined strength) tests: A tool to reduce core damage effects. *Int J Rock Mech Min Sci.* 34(1997):3-4

26. Holt, R.M. et. al, From core compaction to reservoir compaction: Correction for core damage effects. In: SPE/ISRM Eurock '98. Trondheim, Norway, 8-10 July 1998.
27. Holt, R.M., T. Brandshaug, P.A. Cundall, Discrete particle and laboratory modeling of core mechanics. 4th North American Rock Mechanics Symposium, 2000, Girad, Liebman, Breeds, and Doe, eds. Balkema, Rotterdam, 1217 - 1224
28. Meyer, J.P. *Linear failure criteria with three principal stresses*. Thesis, University Of Minnesota. Minneapolis, 2012.
29. Adler, L. Evaluating double elasticity in drill cores under flexure. *Int J Rock Mech Min Sci*. 7(1970): 357-370
30. Itasca, FLAC2D Manuals, V. 7.0, 2012.
31. Bažant, Z.P., J. Planas. 1998. Crack band model and smeared cracking. In *Fracture and Size Effect in Concrete and Other Quasibrittle Materials*, ed. W.F. Chen, 1998, 213-224.
32. Paul, B. A modification of the Coulomb-Mohr theory of fracture. *J App Mech.* 28.2(1961): 259-268
33. Hoek, E., C. Carranza-Torres, B. Corkum. Hoek-Brown failure criterion – 2002 Edition. In: *Proceedings of NARMS-TAC 2002, 5th North American Rock Mechanics Symposium and 17th Tunnelling Association of Canada Conference* – Toronto, Canada – July 7-10, 2002. Vol. 1., pp. 267-271, R. Hammah, W. Bawden, J. Curran and M. Telesnicki, eds. Toronto: University of Toronto Press, 2002
34. Cundall, P. C. Carranza-Torres, R. Hart. A new constitutive model based on the Hoek-Brown criterion. In: *FLAC and Numerical Modeling in Geomechanics – 2003. Proceedings of the 3rd International FLAC Symposium*, Sudbury, Ontario, Canada, October 2003, pp. 321 – 331. R. Brummer et al., eds. Lisse: A.A. Balkema (2003).
35. Vardoulakis I. Shear-band inclination and shear modulus of sand in biaxial tests. *Int J Num Anal Meth Geomech*. 4(1980): 103-109
36. Arthur J.R.F., T. Dunstan, Q Al-Ani, A. Assadi, Plastic deformation and failure in granular material. *Géotechnique*. 27(1977): 53-74
37. Kaiser, P.K., B-H. Kim. Rock mechanics challenges in underground construction and mining. Keynote Lecture. *1st Canada-US Rock Mechanics Symposium*. 2007. 1 - 16
38. Diederichs, M.S., J.L. Carvalho, T.G. Carter. A modified approach for prediction of strength and post yield behavior for high GSI rockmasses in strong, brittle ground. *1st Canada-US Rock Mechanics Symposium.* 2007. 249 – 257

39. Kaiser, P.K., F. Amann, W. Stiner, How highly stressed brittle rock impacts tunnel design. *In: Proceedings of European Rock Mechanics Symposium EUROROCK*. Lausanne, Balkema. 2010.
40. Corkum, A.G., L.J. Lorig, D.O. DeGagné, Continuum representation of brittle rock failure bulking-induced displacements around tunnels. *46th U.S. Rock Mechanics Symposium*. 24 – 27 June. 2012. Chicago, IL.
41. Hajiabdolmajid, V., P.K. Kaiser, C.D. Martin. Modelling brittle failure of rock. *Int J Mech Min Sci*. 39(2002): 731-741.
42. Edelbro, C. Different Approaches for simulating brittle failure in two hard rock mass cases: A parametric study. *Rock Mech Rock Eng*. 43(2010): 151 - 165
43. Zhao, X. M. Cai, M. Cai. Considerations of rock dilation on modeling failure and deformation of hard rocks – a case study of the min-by test tunnel in Canada. *J Rock Mech Geotech Eng*. 2.4(2010): 338-349
44. Vermeer P. A., R. DeBorst. Non-associated plasticity for soils, concrete, and rock. *Heron.* 29(1984): 5-63
45. Zhang, L. *Three-dimensional numerical models of drilling induced fractures*. Thesis, University Of Alberta. Edmonton, 2011.
46. Haimson, B.C, C.G. Herrick. Borehole breakouts and *in situ* stress. In: Proceedings, *12th Annual Energy-Sources Technology Conference and Exhibition, Drilling Symposium.* American Society of Mechanical Engineers, New York. 1989. pgs. 17 – 22
47. Klee, G. et al. In situ stresses in borehole blanche-1/South Australia derived from breakouts, core discing and hydraulic fracturing to 2 km Depth. *Rock Mech Rock Eng*. 44(2011): 531-540

Appendix A – Extra Figures

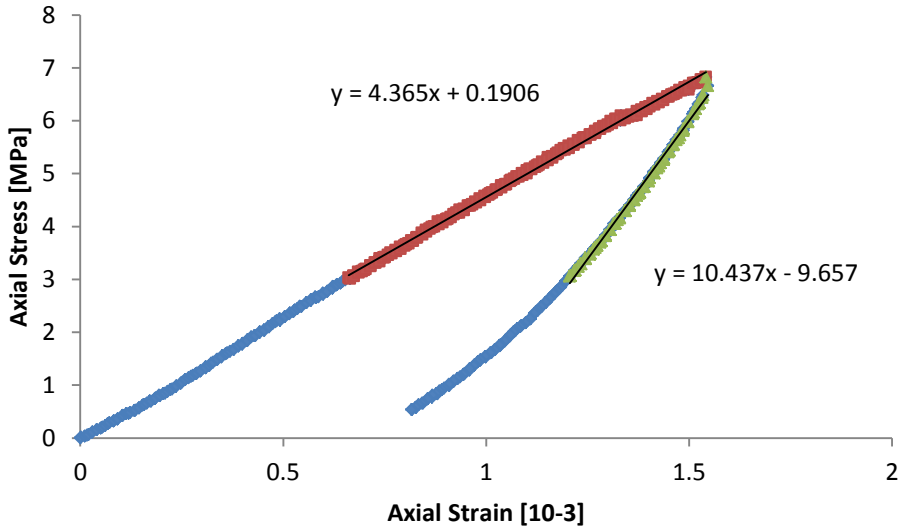

Figure A1: Stress-strain curve for a Core B specimen from a loading condition of 10 MPa.

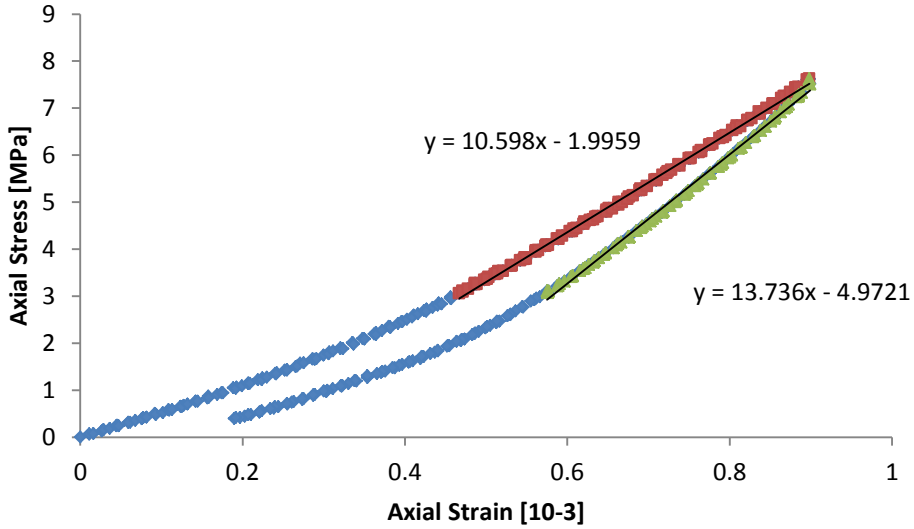

Figure A2: Stress-strain curve for a Core A specimen from a loading condition of 10 MPa.

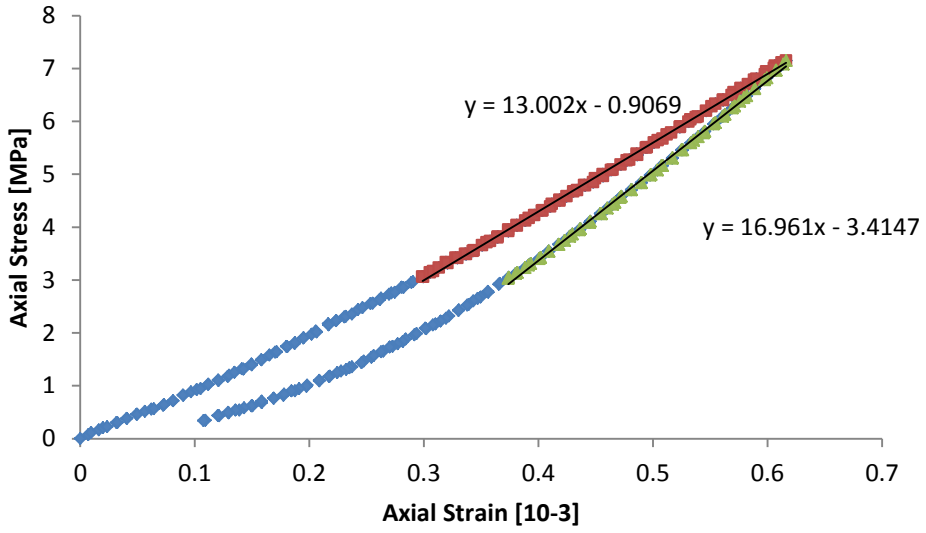

Figure A3: Stress-strain curve for a Core B specimen from a loading condition of 12 MPa.

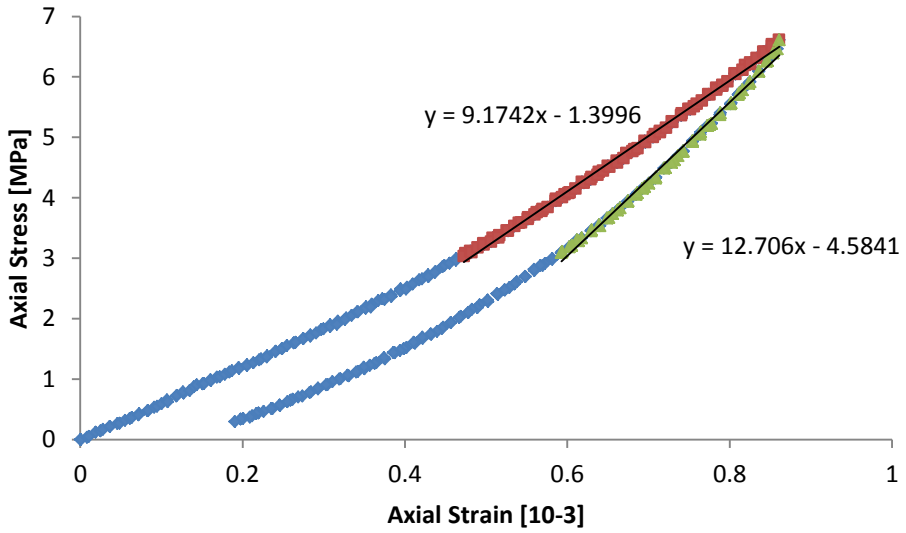

Figure A4: Stress-strain curve for a Core A specimen from a loading condition of 12 MPa.

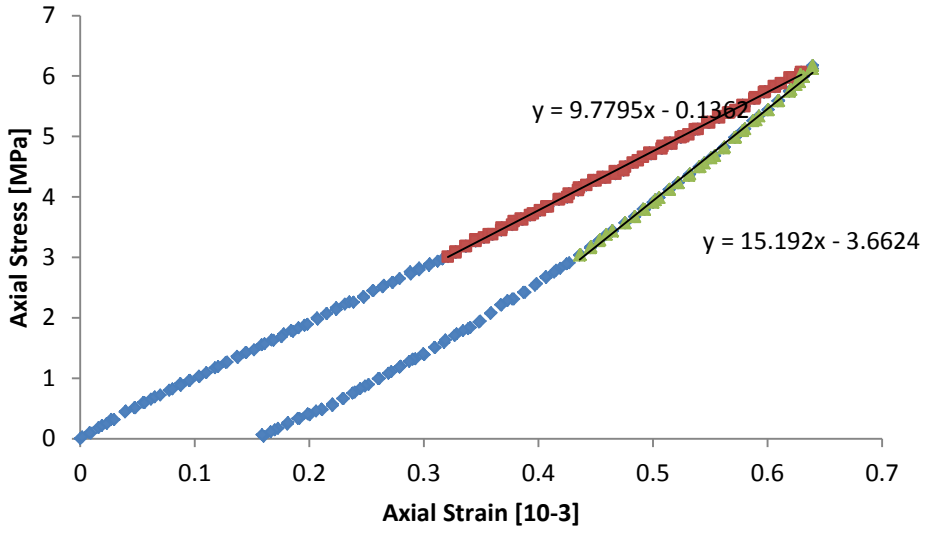

Figure A5: Stress-strain curve for a Core B specimen from a loading condition of 14 MPa.

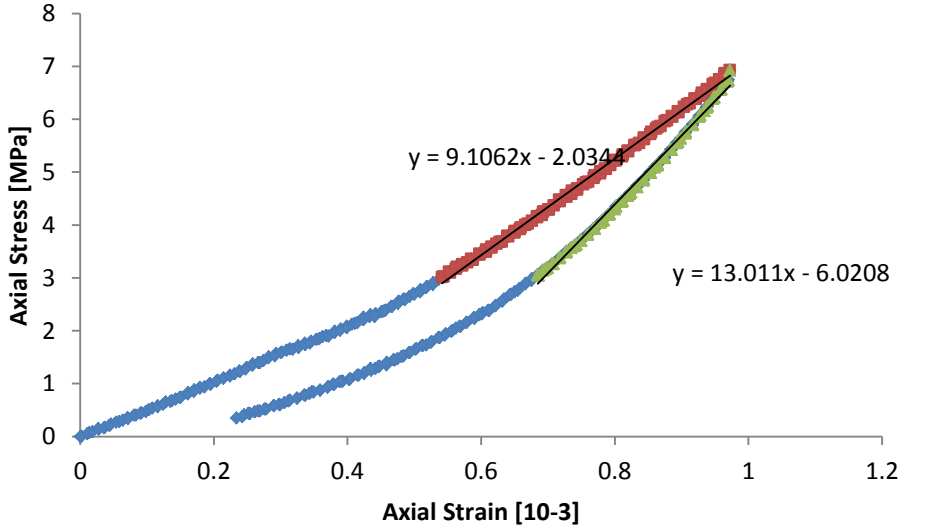

Figure A6: Stress-strain curve for a Core A specimen from a loading condition of 14 MPa.

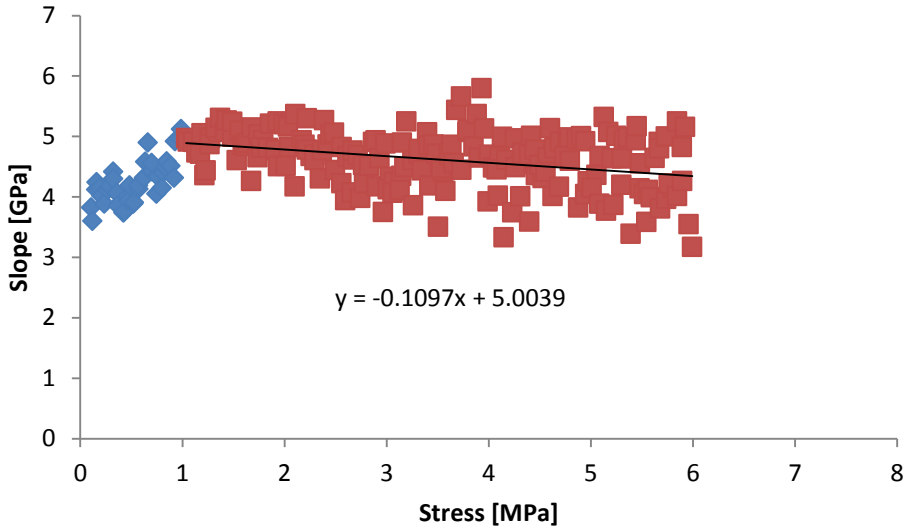

Figure A7: Slope-stress curve for a Core B specimen from a loading condition of 10 MPa.

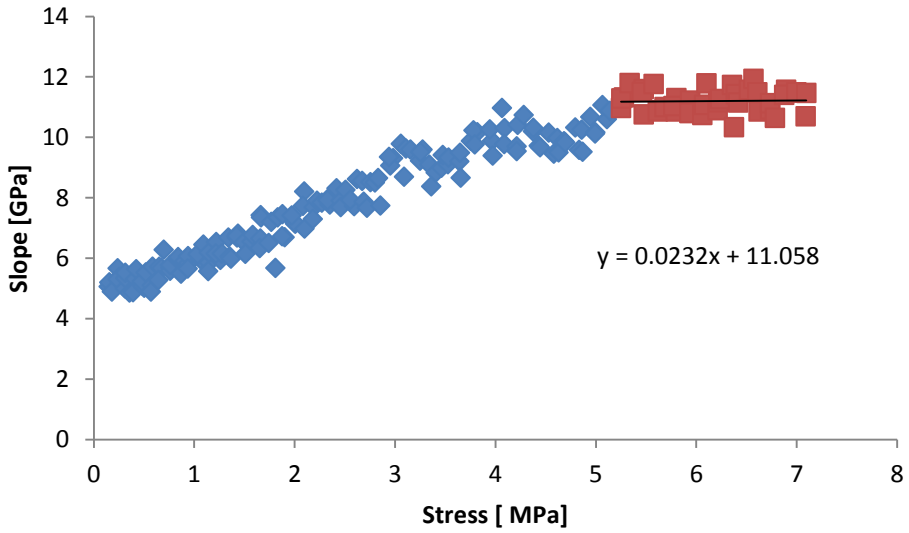

Figure A8: Slope-stress curve for a Core A specimen from a loading condition of 10 MPa.

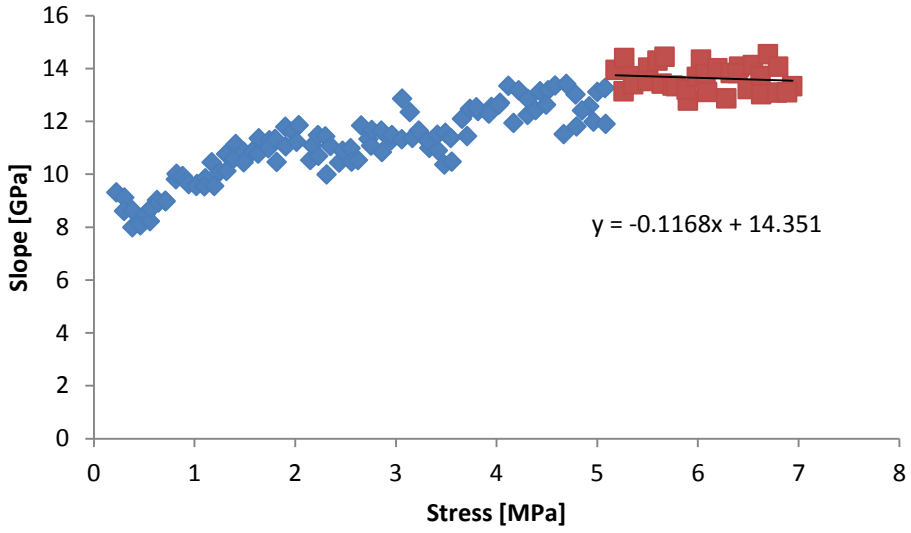

Figure A9: Slope-stress curve for a Core B specimen from a loading condition of 12 MPa.

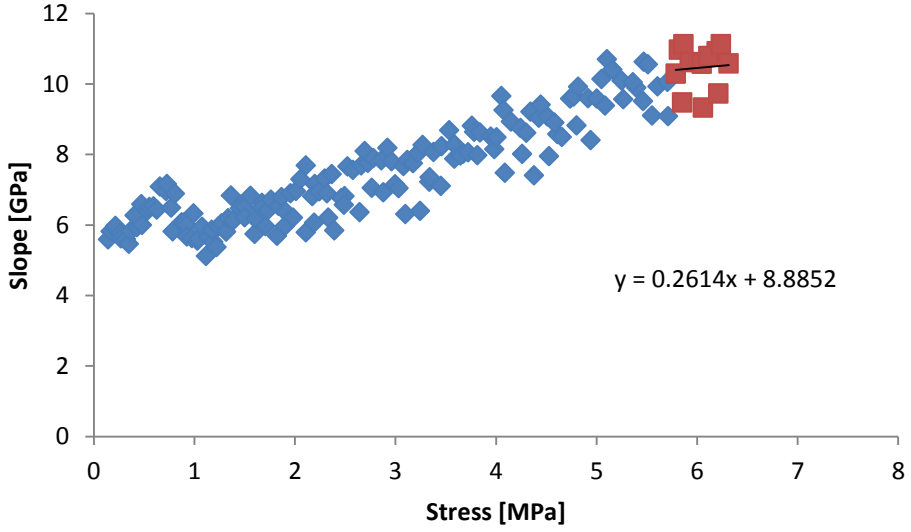

Figure A10: Slope-stress curve for a Core A specimen from a loading condition of 12 MPa.

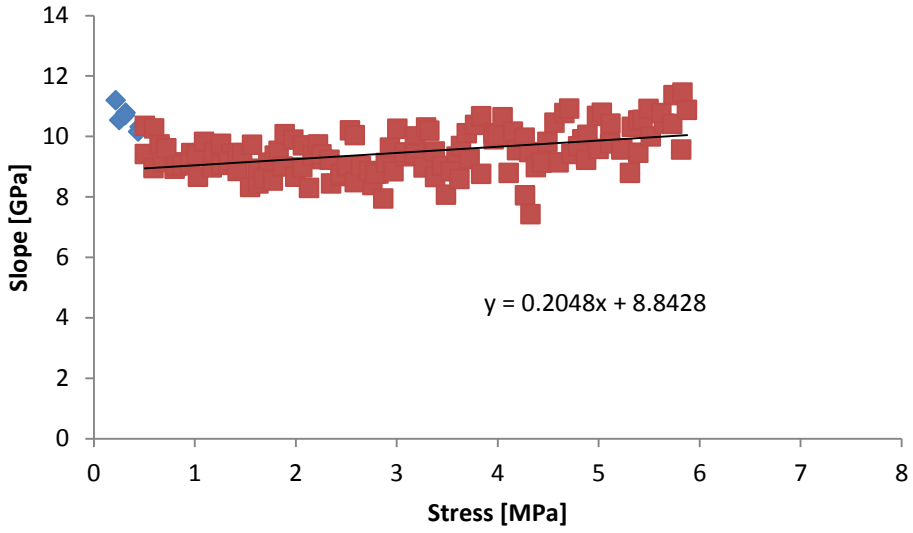

Figure A11: Slope-stress curve for a Core B specimen from a loading condition of 14 MPa.

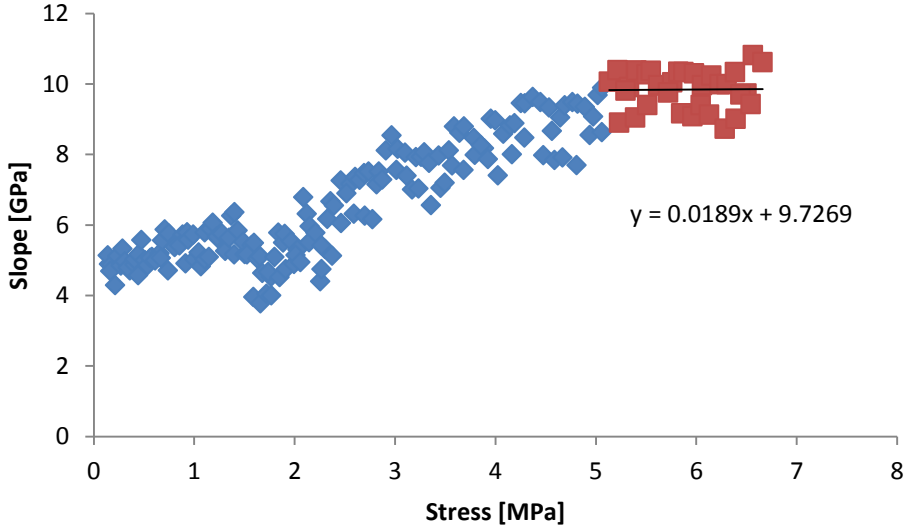

Figure A12: Slope-stress curve for a Core A specimen from a loading condition of 14 MPa.

Appendix B - FLAC CODE

The following code is the basic code used for the core disking analysis. It contains two main sections: initial equilibrium analysis and core disking analysis. The initial equilibrium analysis generates the grid, defines mechanical properties and boundary conditions, and initially runs the system to equilibrium. The core disking analysis defines strength properties and runs the excavation analysis. For the ease of parametric analyses, grid and material values are defined at the beginning of both sections.

Note, this only represents the base code for the analyses. Histories and other commands were implemented when more detailed analysis was required. The elastic and heterogeneity analysis are included following the basic code.

```
;===============================================================
;                        Initial Equilibrium Analysis
;===============================================================
;
;  ===== Define Grid and Elastic Parameters =====
def Parameters
  ; ----- In-situ/Applied Stresses -----
  sxx_ = -55.0e6                          ;Applied Horizontal Stress (Pa)
  ;
  ; ----- Material Properties -----
  YMod_ = 26.0e9                          ;Young's Modulus
  PRat_ = 0.35                            ;Poisson's Ratio
  Den_ = 1000                             ;Density
  ;
  ; ----- Block Dimensions -----
  BlockHeight = 0.34                      ;Height of Block (meters)
  BlockRadius = 0.34                      ;Radius of Block (meters)
  ExcavationDepth1 = 0.085                ;Depth of Excavation (meters)
  CoreRadius = 0.024                      ;Radius of Core (meters)
  ExcWidth = 0.0035 * CoreRadius / 0.016  ;Width of Bit (meters)
  ;
  ; ----- Grid Variables -----
  GridsCorex = 15.0                       ;Grid in Core (x-direction)
  GridsExcx = 4.0                         ;Grids in Bit Path (x-direction)
  GridsBoundx = 50.0                      ;Grids to horizontal external boundary
  GridsBoundy = 40.0                      ;Grids to vertical lower boundary
  Factor = 1.0                            ;Density Factor
  ;
  ; ----- Ratios -----
  RatioyG13 = 0.95
  RatioxG36 = 1.05
  ;
  ; ===== Converstions =====
```

```
  ; ----- Block Dimensions -----
  ExcavationDepth = ExcavationDepth1 * 1.25
  BlockHeight2 = BlockHeight - ExcavationDepth
  ExcRadius = CoreRadius + ExcWidth
  ; ----- Grid and Grid Point Values -----
  G1x2 = GridsCorex / Factor
  G2x1 = G1x2 + 1.0
  G2x2 = G2x1 + GridsExcx / Factor - 1.0
  G3x1 = G2x2 + 1.0
  G3x2 = G3x1 + GridsBoundx - 1.0
  G4x1 = G3x2 + 2.0
  G4x2 = G4x1 + GridsCorex - 1.0
  G5x1 = G4x2 + 1.0
  G5x2 = G5x1 + GridsExcx - 1.0
  GPx12 = G2x1
  GPx23 = G3x1
  GPx3 = G3x2 + 1.0
  GPx4 = G4x1
  GPx45 = G5x1
  GPx5 = G5x2 + 1.0
  Gy3 = GridsBoundy
  Gy5 = 2 * int(GridsCorex * ExcavationDepth / CoreRadius / 2.0)
  G6y1 = Gy3 + 1.0
  G6y2 = G6y1 + Gy5 / Factor - 1.0
  GPy36 = G6y1
  GPy5 = Gy5 + 1.0
  GPy6 = G6y2 + 1.0
  if Gy5 >= G6y2
    Gridtotx = Gy5
  else
    Gridtotx = G6y2
  end_if
  FinExc = 0.25*Gy5
  ; ----- Material Properties -----
  BMod_ = YMod_ / (3.0 * (1.0 - 2.0 * PRat_))
  SMod_ = YMod_ / (2.0 * (1.0 + PRat_))
end
Parameters
;
; ===== Grid Generation =====
config axisymmetry
grid GPx5,Gridtotx
; ----- Grid 1 (lower-left external boundary) -----
gen (0.0,0.0) (0.0,BlockHeight2) (CoreRadius,BlockHeight2) (CoreRadius,0.0) ratio (1,RatioyG13)
i=1,GPx12 j=1,GPy36
; ----- Grid 2 (lower-middle external boundary) -----
gen (CoreRadius,0.0) (CoreRadius,BlockHeight2) (ExcRadius,BlockHeight2) (ExcRadius,0.0) ratio
(1,RatioyG13) i=GPx12,GPx23 j=1,GPy36
; ----- Grid 3 (lower-right external boundary) -----
gen (ExcRadius,0.0) (ExcRadius,BlockHeight2) (BlockRadius,BlockHeight2) (BlockRadius,0.0) ratio
(RatioxG36,RatioyG13) i=GPx23,GPx3 j=1,GPy36
; ----- Grid 4 (Core) -----
```

```
gen (0.0,BlockHeight2) (0.0,BlockHeight) (CoreRadius,BlockHeight) (CoreRadius,BlockHeight2)
i=GPx4,GPx45 j=1,GPy5
; ----- Grid 5 (Excavation Path) -----
gen (CoreRadius,BlockHeight2) (CoreRadius,BlockHeight) (ExcRadius,BlockHeight)
(ExcRadius,BlockHeight2) i=GPx45,GPx5 j=1,GPy5
; ----- Grid 6 (upper-right external boundary)
gen (ExcRadius,BlockHeight2) (ExcRadius,BlockHeight) (BlockRadius,BlockHeight)
(BlockRadius,BlockHeight2) ratio (RatioxG36,1) i=GPx23,GPx3 j=GPy36,GPy6
; ----- Elastic Constitutive Model -----
model elastic i=1,G1x2 j=1,Gy3
model elastic i=G2x1,G2x2 j=1,Gy3
model elastic i=G3x1,G3x2 j=1,Gy3
model elastic i=G4x1,G4x2 j=1,Gy5
model elastic i=G5x1,G5x2 j=1,Gy5
model elastic i=G3x1,G3x2 j=G6y1,G6y2
;  ----- Attach grids -----
attach aside from 1,GPy36 to GPx12,GPy36 bside from GPx4,1 to GPx45,1
attach aside from GPx12,GPy36 to GPx23,GPy36 bside from GPx45,1 to GPx5,1
attach aside from GPx5,1 to GPx5,GPy5 bside from GPx23,GPy36 to GPx23,GPy6
;
; ===== Assign Mechanical Properties =====
prop den = Den_ bulk = BMod_ shear = SMod_
;
; ===== Apply Boundary/Loading Conditions =====
fix  y i 1 GPx3 j 1
ini sxx sxx_ szz sxx_
apply sxx sxx_ from GPx3,GPy6 to GPx3,1
;
; ===== Solve Elastic Analysis =====
Solve
;
;================================================================
;                          Core Disking Analysis
;================================================================
;
;
;  ===== Define Strength Parameters =====
def StrengthVariables
  C_Peak = 26.4e6                          ;Peak Cohesion
  C_Peak2 = C_Peak * 100.0                 ;Amplified Cohesion
  FA_Peak = 52.0                           ;Peak Friction Angle
  T_Peak = 9.1e6                           ;Peak Tensile Strength
  Gf_ = 150.0                              ;Fracture Energy
  Sp_1 = Gf_ / (0.407044*T_Peak*1.3e-3)    ;Residual Plastic Strain for Element Height of
1.3mm
  Sp_ = Sp_1 * 1.3 / 1.6                   ;Residual Plastic Strain
  ;
; ----- Plastic Strain Intervals -----
  E1 = 0.2*Sp_
  E2 = 0.28*Sp_
  E3 = 0.4*Sp_
  E4 = 0.9*Sp_
  E5 = 1.0*Sp_
```

```
end
StrengthVariables
;
; ===== Assign Strain-Softening Constitutive Model =====
model ss i=1,G1x2 j=1,Gy3
model ss i=G2x1,G2x2 j=1,Gy3
model ss i=G3x1,G3x2 j=1,Gy3
model ss i=G4x1,G4x2 j=1,Gy5
model ss i=G5x1,G5x2 j=1,Gy5
model ss i=G3x1,G3x2 j=G6y1,G6y2
;
; ===== Assign Strength Properties =====
; ----- Grid Section 1-3 (CS Model) -----
prop den = Den_ bulk = BMod_ shear = SMod_ i=1,G3x2 j=1,Gy3
prop coh = C_Peak friction = FA_Peak Tension = T_Peak i=1,G3x2 j=1,Gy3
prop ctab 1 ftab 2 ttab 3 i=1,G3x2 j=1,Gy3
;
; ----- Grid Section 5 (CS Model) -----
prop den = Den_ bulk = BMod_ shear = SMod_ i=G5x1,G5x2 j=1,Gy5
prop coh = C_Peak friction = FA_Peak Tension = T_Peak i=G5x1,G5x2 j=1,Gy5
prop ctab 1 ftab 2 ttab 3 i=G5x1,G5x2 j=1,Gy5
;
; ----- Grid Section 6 (CS Model) -----
prop den = Den_ bulk = BMod_ shear = SMod_ i=G3x1,G3x2 j=G6y1,G6y2
prop coh = C_Peak friction = FA_Peak Tension = T_Peak i=G3x1,G3x2 j=G6y1,G6y2 j=1,Gy5
prop ctab 1 ftab 2 ttab 3 i=G3x1,G3x2 j=G6y1,G6y2
;
; ----- Grid Section 4 (TS Model) -----
prop den = Den_ bulk = BMod_ shear = SMod_ i=G4x1,G4x2 j=1,Gy5
prop coh = C_Peak2 friction = FA_Peak Tension = T_Peak i=G4x1,G4x2 j=1,Gy5
prop ttab 3 i=G4x1,G4x2 j=1,Gy5
;
; ----- Plastic Strain Tables -----
table 1 (0.0,C_Peak) (E1,15.0e6) (E2,13.0e6) (E3,10.0e6) (E4,2.5e6) (E5,1.0e6) (1000.0,1.0e6)
table 2 (0.0,FA_Peak) (1000.0,FA_Peak)
table 3 (0.0,T_Peak) (E1,6.17e6) (E2,5.00e6) (E3,4.13e6) (E4,0.5e6) (E5,0.0e6) (1000.0,0.0e6)
;
; ===== Initially Step to Equilibrium =====
step 100
;
; ===== Excavate and Run to Equilibrium =====
def Excavation_
; ----- 50 Excavation Cycles -----
loop n (1,50)
  CurrentExc = Gy5 + 1.0 – n
  ; ----- Excavate and Run to Equilibrium -----
  command
    model null i=G5x1 G5x2 j=CurrentExc
    step 10000
  end_command
  ; ----- Loop through Core (Grid 4) -----
  loop i (G4x1,G4x2)
    loop j (1,Gy5)
```

```
      if tension(i,j) = 0.0
       i_value = i
       j_value = j
       ; ----- Delete Elements that have Tension = 0 -----
       command
         model null i=i_value j=j_value
       end_command
      end_if
    end_loop
  end_loop
end_loop
end
Excavation_
```

The following is the elastic analysis, which will replace the "Core Disking Analysis" section. The only modification to the "Initial Equilibrium Status" is that an extra variable is required during the configuration. This analysis will determine the largest tensile stresses throughout the core, along the core center and boundary along with the location of the element experiencing that stress. The orientation of the major principal stress (or minor principal plane) is included but not integral to this analysis. It can be included during modifications.

To store the values, an extra grid variable is created. Since grid points need to be specified for extra grid variables, the locations of the values follow this pattern. The i-value will correspond to the type of variable. The largest tensile stress throughout the core is stored at G4x1, or the first column in the core. The i- and j- locations of that element are stored in the two columns in increasing value. The largest tensile stress along the core center and its depth then follows. Finally, the largest tensile stress along the core boundary and its depth is stored. The j-value of the grid variable corresponds to the excavation cycle. For example, the row at the top of the element is Gy5. For the first excavation cycle, the values are stored at Gy5. The second excavation cycle is stored at Gy5 – 1.0. This methodology makes analysis quick and conversion to other programs simple.

```
;===========================================================
;                          Elastic Analysis
;===========================================================
;
def ElasticAnalysis
; ----- 50 Excavation Cycles -----
loop n (1,50)
  CurrentExc = Gy5 + 1.0 – n
  ; ----- Excavate and Run to Equilibrium -----
  command
```

```
  model null i=G5x1 G5x2 j=CurrentExc
  step 10000
end_command
;
; ----- Initial Values -----
All_sig3 = 0.0                                  ;Loop through entire core
Cen_sig3 = 0.0                                  ;Loop along core center
Bnd_sig3 = 0.0                                  ;Loop along core boundary
; ----- Storage Locations -----
A_sig3 = G4x1                                   ;largest tensile stress in core
A_i = G4x1 + 1.0                                ;radial distance of element
A_j = G4x1 + 1.0                                ;depth of element
C_sig3 = G4x1 + 1.0                             ;largest tensile stress along core center
C_j = G4x1 + 1.0                                ;depth of element
B_sig3 = G4x1 + 1.0                             ;largest tensile stress along core boundary
B_j = G4x1 + 1.0                                ;depth of element
;
; ===== Loop Through Entire Core =====
loop i (G4x1,G4x2)
  loop j (1,Gy5)
    sig_xx = sxx(i,j)                           ;xx-stress
    sig_yy = syy(i,j)                           ;yy-stress
    sig_xy = sxy(i,j)                           ;xy-stress
    sig_c = 0.5*(sig_xx + sig_yy)               ;center of mohr's circle
    sig_r = sqrt((0.5*(sig_xx - sig_yy))^2+(sig_xy)^2)  ;radius of mohr's circle
    sig_1 = sig_c - sig_r                       ;major principal stress
    sig_3 = sig_c + sig_r                       ;minor principal stress
    angle_ten0 = atan2(-2*sig_xy,sig_yy - sig_xx)
    angle_ten1 = 0.5 * angle_ten0 *180 / pi     ;orientation of sig1
    ; ----- If Sig3 is larger than stored value, replace -----
    if sig_3 > All_sig3
      All_sig3 = sig_3
      All_i = i
      All_j = j
    end_if
  end_loop
end_loop
ex_1(A_sig3,CurrentExc) = All_sig3
ex_1(A_i,CurrentExc) = All_i
ex_1(A_j,CurrentExc) = All_j
; ===== Loop Along Core Center =====
loop j (1,Gy5)
  sig_xx = sxx(G4x1,j)                          ;xx-stress
  sig_yy = syy(G4x1,j)                          ;yy-stress
  sig_xy = sxy(G4x1,j)                          ;xy-stress
  sig_c = 0.5*(sig_xx + sig_yy)                 ;center of mohr's circle
  sig_r = sqrt((0.5*(sig_xx - sig_yy))^2+(sig_xy)^2)  ;radius of mohr's circle
  sig_1 = sig_c - sig_r                         ;major principal stress
  sig_3 = sig_c + sig_r                         ;minor principal stress
  ; ----- If Sig3 is larger than stored value, replace -----
  if sig_3 > Cen_sig3
    Cen_sig3 = sig_3
    Cen_j = j
```

```
  end_if
 end_loop
 ex_1(C_sig3,CurrentExc) = Cen_sig3
 ex_1(C_j,CurrentExc) = Cen_j
 ; ===== Loop Along Core Boundary =====
 loop j (1,Gy5)
  sig_xx = sxx(G4x2,j)                                    ;xx-stress
  sig_yy = syy(G4x2,j)                                    ;yy-stress
  sig_xy = sxy(G4x2,j)                                    ;xy-stress
  sig_c = 0.5*(sig_xx + sig_yy)                           ;center of mohr's circle
  sig_r = sqrt((0.5*(sig_xx - sig_yy))^2+(sig_xy)^2)      ;radius of mohr's circle
  sig_1 = sig_c - sig_r                                   ;major principal stress
  sig_3 = sig_c + sig_r                                   ;minor principal stress
  ; ----- If Sig3 is larger than stored value, replace -----
  if sig_3 > Cen_sig3
   Bnd_sig3 = sig_3
   Bnd_j = j
  end_if
 end_loop
 ex_1(B_sig3,CurrentExc) = Bnd_sig3
 ex_1(B_j,CurrentExc) = Bnd_j
end_loop
end
ElasticAnalysis
```

The following is the heterogeneity analysis, which replaces the "Core Disking Analysis". Similar to the elastic analysis, an extra grid variable is required. Since the tensile strength is varied, the table command cannot be used for softening. This forces the user to code the softening themselves. The extra grid variable stores the initial tensile strength value for each element to be used later.

```
;=============================================================
;                        Heterogeneity Analysis
;=============================================================
;
;
;  ===== Define Strength Parameters =====
def StrengthVariables
 C_Peak = 26.4e6                          ;Peak Cohesion
 C_Peak2 = C_Peak * 100.0                 ;Amplified Cohesion
 FA_Peak = 52.0                           ;Peak Friction Angle
 T_Peak = 9.1e6                           ;Peak Tensile Strength
 Dev_ = 10.0                              ;Deviation Percentage
 T_Dev = T_Peak * Dev_ / 100.0            ;Tensile Strength Deviation
 Gf_ = 150.0                              ;Fracture Energy
 Sp_1 = Gf_ / (0.407044*T_Peak*1.3e-3)    ;Residual Plastic Strain for Element Height of
1.3mm
 Sp_ = Sp_1 * 1.3 / 1.6                   ;Residual Plastic Strain
 ;
; ----- Plastic Strain Intervals -----
```

```
  E1 = 0.2*Sp_
  E2 = 0.28*Sp_
  E3 = 0.4*Sp_
  E4 = 0.9*Sp_
  E5 = 1.0*Sp_
end
StrengthVariables
;
; ===== Assign Strain-Softening Constitutive Model =====
model ss i=1,G1x2 j=1,Gy3
model ss i=G2x1,G2x2 j=1,Gy3
model ss i=G3x1,G3x2 j=1,Gy3
model ss i=G4x1,G4x2 j=1,Gy5
model ss i=G5x1,G5x2 j=1,Gy5
model ss i=G3x1,G3x2 j=G6y1,G6y2
;
; ===== Assign Strength Properties =====
; ----- Grid Section 1-3 (CS Model) -----
prop den = Den_ bulk = BMod_ shear = SMod_ i=1,G3x2 j=1,Gy3
prop coh = C_Peak friction = FA_Peak Tension = T_Peak i=1,G3x2 j=1,Gy3
prop ctab 1 ftab 2 ttab 3 i=1,G3x2 j=1,Gy3
;
; ----- Grid Section 5 (CS Model) -----
prop den = Den_ bulk = BMod_ shear = SMod_ i=G5x1,G5x2 j=1,Gy5
prop coh = C_Peak friction = FA_Peak Tension = T_Peak i=G5x1,G5x2 j=1,Gy5
prop ctab 1 ftab 2 ttab 3 i=G5x1,G5x2 j=1,Gy5
;
; ----- Grid Section 6 (CS Model) -----
prop den = Den_ bulk = BMod_ shear = SMod_ i=G3x1,G3x2 j=G6y1,G6y2
prop coh = C_Peak friction = FA_Peak Tension = T_Peak i=G3x1,G3x2 j=G6y1,G6y2 j=1,Gy5
prop ctab 1 ftab 2 ttab 3 i=G3x1,G3x2 j=G6y1,G6y2
;
; ----- Grid Section 4 (TS Model) -----
prop den = Den_ bulk = BMod_ shear = SMod_ i=G4x1,G4x2 j=1,Gy5
prop coh = C_Peak2 friction = FA_Peak Tension = T_Peak rdev = T_Dev i=G4x1,G4x2 j=1,Gy5
prop ttab 3 i=G4x1,G4x2 j=1,Gy5
;
; ----- Plastic Strain Tables -----
table 1 (0.0,C_Peak) (E1,15.0e6) (E2,13.0e6) (E3,10.0e6) (E4,2.5e6) (E5,1.0e6) (1000.0,1.0e6)
table 2 (0.0,FA_Peak) (1000.0,FA_Peak)
table 3 (0.0,T_Peak) (E1,6.17e6) (E2,5.00e6) (E3,4.13e6) (E4,0.5e6) (E5,0.0e6) (1000.0,0.0e6)
;
; ===== Initially Step to Equilibrium =====
step 100
;
; ===== Store Tensile Strength Values as Extra Grid Variable =====
def tenstrength
 loop i (1,izones)
   loop j (1,jzones)
     ex_1(i,j) = tension(i,j)
   end_loop
 end_loop
end
```

```
tenstrength
;
;
; ===== Define Function for Tensile Softening =====
def tensoft
; ----- Loop Through Elements in Core -----
loop i (G4x1,G4x2)
  loop j (1,Gy5)
    i_val = i
    j_val = j
    TT1 = ex_1(i,j)
    TT2 = 0.678022*T_Peak
    TT3 = 0.549451*T_Peak
    TT4 = 0.453846*T_Peak
    TT5 = 0.054945*T_Peak
    TT6 = 0.0
    E_t = et_plastic(i,j)
    $E_t = E_t
    $Et_Pre = tension(i,j)
    ;
    ; ----- Interpolate Tensile Strength based on Plastic Tensile Strain -----
    if E_t < E1
      tension(i,j) = TT1 - (TT1 - TT2)/(E1 - 0.0)*(E_t - 0.0)
    else
      if E_t < E2
        tension(i,j) = TT2 - (TT2 - TT3)/(E2 - E1)*(E_t - E1)
      else
        if E_t < E3
          tension(i,j) = TT3 - (TT3 - TT4)/(E3 - E2)*(E_t - E2)
        else
          if E_t < E4
            tension(i,j) = TT4 - (TT4 - TT5)/(E4 - E3)*(E_t - E3)
          else
            if E_t < E5
              tension(i,j) = TT5 - (TT5 - TT6)/(E5 - E4)*(E_t - E4)
            else
              tension(i,j) = 0.0
              et_plastic(i,j) = E5 + 1.0
              $Et_post = tension(i,j)
              command
                model null i=i_val j=j_val
              end_command
            end_if
          end_if
        end_if
      end_if
    end_if
  end_loop
 end_loop
end
;
; ===== Define Step Function =====
def sstep
```

```
  tensoft
  command
    step 10
  end_command
end
;
; ===== Excavate and Run to Equilibrium =====
def ssolve
 loop n (1,44)
   CurrentExc = Gy5 + 1.0 - n
   command
     model null i=G5x1 G5x2 j=CurrentExc
   end_command
   loop k (1,nss)
     sstep
   end_loop
 end_loop
end
set echo off mess off
set nss=1000                                                    ;Number cycles for step function
ssolve
```